Reverberation Mapping Analysis of the 2016 HST Campaign on NGC 4593

Lukas Diehl

George-August-Universität Göttingen

February 4, 2026

Abstract

Abstract

Contents

List of Figures

List of Tables

1. Introduction

Active galactic nuclei (AGNs) are among the most luminous objects in the universe, emitting radiation across the entire electromagnetic spectrum (Netzer 2013). In contrast to inactive galaxies such as the Milky Way, the supermassive black hole (SMBH) in an active galaxy continues to accrete matter from its central region. This process produces thermal emission from the accretion flow (Peterson 1997) and drives line emission through photoionization and subsequent recombination in the surrounding gas (Netzer 2013). AGNs exhibits strong variability across the electromagnetic spectrum, with timescales ranging from hours to days (Ulrich et al. 1997).

An interesting example of this class of objects is the barred spiral galaxy NGC 4593. It shows pronounced variability from the X-ray to the optical bands (McHardy et al. 2017; Cackett et al. 2018) and exhibits several prominent broad emission lines, including Balmer and helium lines, as well as low-ionization lines like O I $\lambda 8446$ (Kollatschny & Dietrich 1997; Cackett et al. 2018; Ochmann et al. 2025). Several studies have analysed the structure and kinematics of NGC 4593 (e.g. (Kollatschny & Dietrich 1997; Denney et al. 2006; Cackett et al. 2018)) using reverberation mapping (RM) of the broad emission lines. This method uses measurable time delays between variations in the ionizing continuum and the response of the line-emitting gas to infer the characteristic size and geometry of the broad-line region (Peterson 1993).

In a recent study, Cackett et al. 2018 carried out an observation campaign using the Hubble Space Telescope (HST) with the Space Telescope Imaging Spectrograph (STIS), between 12 July and 6 August 2016 on NGC 4593, covering wavelength ranges of approximately $1100\,\text{Å} - 1700\,\text{Å}$ and $3900\,\text{Å} - 9000\,\text{Å}$. This campaign focused on the reverberation of the accretion disk of NGC 4593 by analyzing the UV and optical continua (Cackett et al. 2018). Based on this campaign, this thesis presents a classical RM analysis of the broad emission lines and derives an estimate of the SMBH mass.

Furthermore, NGC 4593 shows prominent emission in the low-ionization O I $\lambda 8446$ line and the Ca II $\lambda 8498\,\lambda 8542\,\lambda 8662$ triplet (Ochmann et al. 2025), which have rarely

been included in RM campaigns so far. The Oi $\lambda 8446$ line is particularly interesting because its strength can be enhanced by Bowen fluorescence(Bowen 1947; Grandi 1980). Since it is covered by the Cackett et al. 2018 campaign, its variability and time lag to can be measured from a HST/STIS RM campaign for the first time.

2. Scientific Background

2.1 Active Galactic Nuclei

Active Galactic Nuclei (AGNs) refer to the central region of active galaxies. These objects are among the most luminous in the universe, with bolometric luminosities ranging from 10^{41} to 10^{48} erg s^{-1}, outshining entire galaxies by several orders of magnitude (Peterson 1997). Historically, several stellar-based models were proposed, such as dense star clusters or supermassive stars. However, these scenarios were discarded, as they are expected to collapse into black holes themselves, and they cannot provide the required energy output. Today, it is understood that the enormous luminosities of AGN are powered by accretion of matter onto a supermassive black hole (SMBH) at the centers of galaxies (Rees 1984). The most widely accepted model for this accretion is a hot, rotating accretion disk surrounding the SMBH, which produces most of the observed radiation (Shakura & Sunyaev 1973). The following sections will outline the key components of an AGN and its variability, which is central to reverberation mapping analysis.

Figure 2.1: Different components of an AGN. Adopted from (Mo et al. 2010) Figure 14.3.

2.1.1 Structure and Spectral Features of an AGN

Figure 2.1 shows a schematic illustration of an AGN, consisting of a central super-massive black hole (SMBH), a surrounding accretion disk, a dusty torus and ionized gas regions known as the broad-line region (BLR) and narrow-line region (NLR). In some cases, relativistic jets are launched perpendicular to the plane of the accretion disk (Urry & Padovani 1995). The following subsections describe the physical components of AGN and the spectral features associated with them.

Supermassive Black Hole and Accretion Disk

The center of an AGN is defined by a supermassive black hole (SMBH), with typical masses between $10^6 \, M_\odot$ and $10^9 \, M_\odot$ (Peterson et al. 2004). It does not contribute to the AGN spectrum directly, but acts as the central engine driving observed spectral features of the AGN. It dominates the gravitational potential and, unlike inactive galaxies such as the Milky Way, it is surrounded by an accretion disk. Through viscous processes within the disk, such as turbulent friction and magneto-rotational instability, the angular momentum of the matter is transported outward, which leads to a spiraling inflow of matter toward the SMBH (Shakura & Sunyaev 1973). Several models have been proposed to describe the accretion process. The most widely used model is the geometrically thin and optically thick accretion disk, which consists of ionized gas in differential rotation around the SMBH (Shakura & Sunyaev 1973; Netzer 2013). The disk is composed primarily of ionized hydrogen and helium, with trace amounts of heavier elements (Netzer 2013). It extends from the innermost stable circular orbit (ISCO) near the event horizon out to distances of several light-days. The radial extent of the disk is relatively small compared to galactic scales and typically ranges from a few light-hours to a few light-days, corresponding to about 10^{-3} to 10^{-2} pc (Shakura & Sunyaev 1973; Netzer 2013).

During the accretion process a substantial fraction of the gravitational energy of the matter is transformed into thermal radiation, which accounts for the enormous luminosity observed in AGNs and heats the accretion disk to high temperatures that depend on the mass of the SMBH (Netzer 2013). For example, the maximum effective temperature for an accretion disk around a SMBH with $M = 10^8, M_\odot$ is on the order of several $\times 10^5$ K, leading to UV and optical emission (Shakura & Sunyaev 1973; Netzer 2013). By contrast, disks around stellar-mass black holes reach much higher temperatures (up to a few $\times 10^6$ K), and therefore emit mostly in X-rays (Shakura & Sunyaev 1973; Netzer 2013). Due to the radial temperature gradient, the emitted spectrum cannot be described as a single blackbody. Instead, it results

from a superposition of many blackbody-like components at different temperatures, often referred to as a multicolour black-body (Netzer 2013). This produces a broad optical–UV continuum of ionizing photons, which interact with gas clouds near the nucleus and play a crucial role in shaping the spectral features of the BLR and NLR. These photons cause photoionization followed by recombination, which gives rise to the strong emission lines that are characteristic of AGN spectra (Netzer 2013).

Broad-Line and Narrow-Line Region

The ionized gas clouds near the nucleus can be divided into the broad-line region (BLR) and the narrow-line region (NLR). Both regions differ in density, distance from the SMBH, and the observed line widths (Urry & Padovani 1995). The BLR is located close to the nucleus, at distances ranging from a few light-days to a few light-years from the central SMBH (Goad et al. 2012)(see Figure 2.1). It consists of dense gas clouds with electron densities of $n_e \approx 10^{11}\,\mathrm{cm}^{-3}$, moving at velocities of several thousand $\mathrm{km\,s}^{-1}$ due to the strong gravitational influence of the SMBH. These velocities lead to significant Doppler broadening of permitted emission lines, with widths of $(500\text{–}10{,}000)\,\mathrm{km\,s}^{-1}$ (Peterson 1997). As described earlier, the BLR is photoionized by the continuum radiation emitted from the accretion disk. Consequently, the line emission from this region responds to changes in the continuum, leading to a strong correlation between the two and strong variability (Netzer 2013). This relationship is particularly relevant for reverberation mapping, which will be discussed later in Section 2.2.
Modelling the geometry of the BLR is challenging, because several emission lines have to be considered, whose intensities vary in response to changes in the continuum radiation (Netzer 2013). A common model assumes a spherical distribution of clouds connected to the accretion disk and located between the accretion disk and the dusty torus (Goad et al. 2012). Broad emission lines arise from permitted transitions such as Hα, Hβ, and Lyα (Netzer 2013).

The narrow-line region (NLR) extends out to several hundred parsecs from the central region (Peterson 1997). The gas in this region moves at much lower velocities, resulting in emission lines with widths typically of order $(350\text{–}400)\,\mathrm{km\,s}^{-1}$ (Peterson 1997). In contrast to the BLR, the NLR exhibits both permitted and forbidden transitions. Forbidden lines, such as [O III] $\lambda5007$, are prominent in the NLR because at its low densities ($n_e \sim 10^2\text{–}10^4\,\mathrm{cm}^{-3}$) collisional de-excitation is rare, allowing radiative decay from metastable levels (Peterson 1997). Due to its much larger extent compared to the BLR, the NLR responds only very slowly to

variations in the ionizing continuum. Therefore, the flux of the narrow emission lines can be treated as constant over timescales of several years (Peterson 1993).

Because permitted emission lines can originate in both the BLR and the NLR, they often exhibit a multi-component line profile consisting of a broad and a narrow component (Peterson 1997). The relative strength of the broad and narrow components depends on the fractional contribution of emission from the BLR and the NLR, respectively(Peterson 1997).

Dusty Torus

Surrounding the accretion disk and the broad-line region is the dusty torus, a geometrically thick, optically dense structure composed of gas and dust. It extends from the radius at which dust can survive the intense radiation from the accretion disk out to scales of a few parsecs (Netzer 2013). The torus likely has a clumpy distribution and plays a crucial role in the unified model of AGNs (Urry & Padovani 1995; Netzer 2013). The dust in the torus absorbs a significant fraction of the UV and optical radiation emitted by the accretion disk and re-emits it thermally in the infrared. As a result, AGNs typically exhibit strong infrared emission, with the peak wavelength depending on the dust temperature in the torus (Netzer 2013). Even when the central region is hidden from direct view by the torus, this reprocessed infrared emission remains observable. It therefore provides a characteristic signature of obscured AGN activity and enables indirect constraints on the otherwise hidden central engine (Netzer 2013).

2.1.2 Classification

AGNs get classified in subgroups based on their spectral features, which are strongly dependent to their intrinsic structure. The key parameters for this classification are luminosity, emission-line profiles and radio properties. Based on those parameters AGN get grouped into Seyfert galaxies, quasars and radio galaxies (Peterson 1997). They get further subdivided based on the appearance of broad and narrow emission lines. Some examples for these sub-classes are narrow-line Seyfert I galaxies (NLS1s), low-ionization nuclear emission-line regions (LINERs), and jet-dominated sources such as BL Lac objects or blazars (Antonucci 1993; Urry & Padovani 1995).

Figure 2.2: An example of Seyfert I and Seyfert II spectra illustrating their differences. Broad lines, such as the highlighted $H\alpha$ and $H\beta$, are only present in the Seyfert I spectrum, whereas forbidden [O III] lines are visible in both cases. Adapted from (Keel 2002).

Seyfert Galaxies

Seyfert galaxies are named after Carl K. Seyfert, who in 1943 observed spiral galaxies characterized by exceptionally bright nuclei and strong emission lines in their optical spectra (Seyfert 1943). They are mainly classified into the sub-classes Seyfert I and Seyfert II based on the presence of broad emission lines (Peterson 1997). Figure 2.2 highlights the differences of the spectra of Type I and Type II Seyfert galaxies.

Seyfert I galaxies, show both broad and narrow emission lines in their optical spectra. Broad lines (e.g the Balmer line $H\alpha$) typically exhibits full widths at half maximum (FWHM) of several thousand kilometers per second and emerge from the fast-moving, high-density gas in the BLR (Peterson 1997). In contrast, narrow lines, including prominent forbidden transitions like [O III] $\lambda 5007$ or [N II] $\lambda 6584$, originate from the slow-moving, low-density gas in the NLR (Peterson 1997). An AGN showing both components in its spectrum is classified as a Seyfert 1 galaxy (Peterson 1997), as is the case which is the case for NGC 4593. Further details on NGC 4593 are provided in Section 3.1. Between the two main Seyfert classes, several intermediate subclasses (1.2, 1.5, 1.8, 1.9) are defined based on the relative strength of the broad and narrow Balmer-line components in the optical spectrum (Osterbrock 1977; Osterbrock 1981; Peterson 1997). Seyfert 1.8 and 1.9 galaxies show very weak broad components. In Seyfert 1.9 objects, the broad component is

visible only in the Hα line, whereas in Seyfert 1.8 objects it is also detectable in Hβ. Furthermore, if the broad and narrow components in Hβ are of equal strength, the AGN is classified as a Seyfert 1.5 (Peterson 1997). If the narrow component is even weaker than the broad component, it is classified as a Seyfert 1.2 (Osterbrock 1977).

Seyfert II galaxies lack broad-line emission in their optical spectra, most likely due to orientation-dependent obscuration by a dusty torus (Antonucci 1993; Peterson 1997).This implies that the classification of Seyfert galaxies depends strongly on the observer's viewing angle, which is a central element of the unified model of AGN (Antonucci 1993; Peterson 1997). The unified model is discussed in more detail in Section 2.1.3.

Another notable subclass of Seyfert Galaxies are narrow-line Seyfert I galaxies (NLS1s). They show most of the features of Seyfert 1 or 1.5 galaxies, except that the usually broad lines (e.g the Balmer lines), exhibit FWHM values that are only slightly larger than those of the narrow lines (Osterbrock & Pogge 1985). They show a wide dispersion of spectral properties, with some objects have very strong Fe II emission, whereas others show almost none. This indicates that NLS1s do not form a homogeneous class (Osterbrock & Pogge 1985).

Additional AGN Classes

In addition to Seyfert galaxies, there are several other classes of AGNs. Quasars (quasi-stellar objects) are more luminous than Seyfert galaxies, typically outshine their host galaxies, and are usually observed at higher redshifts (Netzer 2013). Because quasars show emission properties similar to those of Seyfert galaxies, the modern distinction is primarily based on luminosity: quasars are high-luminosity AGNs, whereas Seyfert galaxies occupy the lower-luminosity end (Netzer 2013).

Radio galaxies form another important AGN class, distinguished by their strong radio emission and prominent jets and are typically found in elliptical host galaxies (Netzer 2013). When their jets are aligned close to the observers line of sight, they are observed as blazars or BL Lac objects, which exhibit rapid variability and featureless optical spectra due to relativistic beaming (Netzer 2013).

Finally, LINERs are low-luminosity AGNs with spectra dominated by low-ionization emission lines. The physical origin of their ionization mechanism is still debated, and in some cases, they may not be powered by accretion at all (Netzer 2013).

While these classifications are based primarily on spectral characteristics, many of the observed differences between AGN types can be attributed to orientation ef-

fects. The Unified Model of AGN provides a framework that explains this apparent diversity through a common internal structure, viewed from different angles.

2.1.3   Unification Model

Figure 2.3 illustrates the unified model of AGN proposed by Antonucci 1993. He argued that the observed differences among AGN spectra do not require fundamentally different intrinsic structures. Instead, they arise mainly from orientation of the central region towards the observer and from its obscuration by the dusty torus (Antonucci 1993).

The figure shows how the same AGN would be classified depending on the observer's viewing angle. As mentioned above, the dusty torus plays a key role, as it surrounds the SMBH, the accretion disk and the fast-moving BLR. If the line of sight is blocked by the torus, the broad-line emission is obscured, resulting in a Seyfert II spectrum, exhibiting only narrow emission lines. In this geometry, the AGN is viewed at high inclination, with the torus intercepting the line of sight. If, on the other hand, the nucleus is viewed directly and is not obscured by the torus, both broad and narrow emission lines are observed in the spectrum, and the AGN is classified as a Seyfert I galaxy (Urry & Padovani 1995).

The same principle applies to other AGN classes. Quasars can be considered the high-luminosity counterparts of Seyfert galaxies, where orientation and torus obscuration likewise affect their observed properties. Blazars, are seen when the relativistic jet is aligned closely with the observer's line of sight, leading to strong Doppler boosting, which makes the radiation appear significantly brighter and shifted to higher frequencies than it intrinsically is (Urry & Padovani 1995).

Although the classical Unification Model treats AGN classification as fixed and purely geometry-driven, some AGNs have been observed to change their spectral type over time (Ricci & Trakhtenbrot 2023). These so-called "changing-look AGNs" demonstrate that a purely orientation-based interpretation, such as the Unification Model, cannot explain all observed phenomena. They suggest that intrinsic changes, such as variations in accretion rate or obscuring material, can also affect the classification (Ricci & Trakhtenbrot 2023).

2.1.4   Variability

The variability of active galactic nuclei (AGNs) is one of the key aspects that enables the study of their central regions, which generally cannot be probed with conventional spatially resolved observations. Variability is observed on timescales ranging
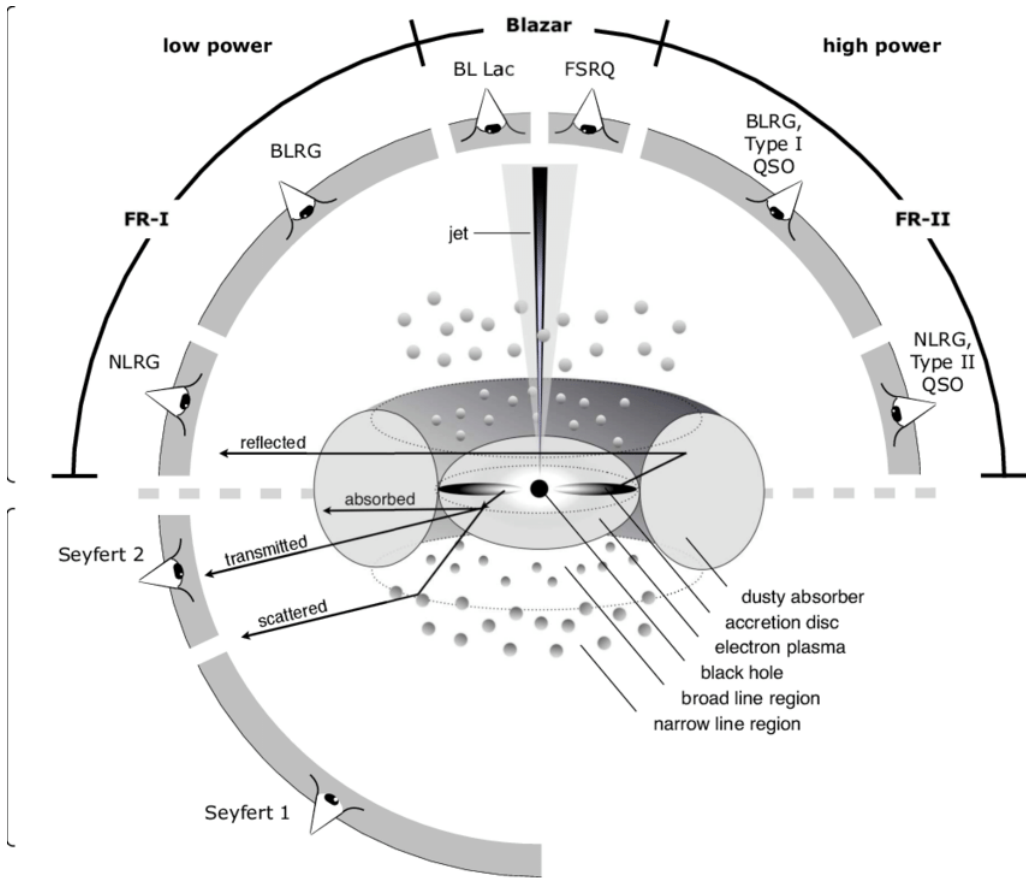
Figure 2.3: This graphic shows a schematic of the unification model of an AGN. The figure was adopted from (Beckmann & Shrader 2013).

from hours to several years and is generally stochastic, resulting in flux variations of both emission lines and continuum emission of up to a few tens of percent in the UV and optical bands (Ulrich et al. 1997; Ochmann et al. 2024). Although the origin of this variability is not yet fully understood, the most widely accepted models attribute it to inhomogeneities and instabilities within the accretion disk (Ulrich et al. 1997; Dexter & Agol 2010).

Depending on the underlying physical process, variations occur on different characteristic timescales. Processes such as thermal fluctuations or changes in the accretion flow happen on timescales of decades to centuries for typical SMBH masses and radii, and are therefore difficult to observe directly. In contrast, processes operating on shorter timescales are easier to study. Examples include gas motions and mechanical instabilities (e.g., sound waves) within the disk, which occur on timescales of weeks to months (Ricci & Trakhtenbrot 2023). The shortest timescale is the light-crossing timescale, $t_{lc} = R/c$, which specifies how long light takes to traverse the emitting region (e.g., the broad-line region, BLR) (Ricci & Trakhtenbrot 2023).

Here, c denotes the speed of light, and R denotes the characteristic size or radius of the variable emitting region. Following Ricci & Trakhtenbrot 2023, assuming a SMBH of mass $\approx 10^8 \, M_\odot$, the light-crossing timescale can be written as

$$t_{\mathrm{lc}} = \frac{R}{c} \simeq 0.87 \left(\frac{R}{150 \, r_g} \right) M_8 \, \mathrm{days}, \tag{2.1}$$

where $r_g = GM/c^2$ is the gravitational radius of the black hole. Thus, the light-crossing timescale of the variable emitting region is of order days, and t_{lc} scales linearly with the size of the emitting region (Ricci & Trakhtenbrot 2023).

Because variations in the ionizing continuum occur on such short timescales, it is possible to measure delayed responses from other regions within the AGN that are correlated with the continuum, using long-term monitoring campaigns (Peterson 1997). In particular, the BLR responds to changes in the photoionizing continuum radiation of the central source with a time delay (lag) that is longer than the light-crossing timescale of the emitting region (Peterson 1997). This lag forms the basis of classical reverberation mapping, which will be further elaborated in the next section.

2.2 Reverberation Mapping

The main focus of this work is a classical reverberation mapping analysis of the broad lines of NGC 4593. Reverberation mapping probes the structure of the BLR around the SMBH by measuring the time delay (lag) between continuum variations and the correlated response of the broad lines. This lag can be used to constrain the BLR geometry and to estimate the SMBH mass (Cackett et al. 2018).

2.2.1 Principle of Reverberation Mapping

The fundamental assumption in reverberation mapping is that variations in the observed continuum flux are echoed by variations in the emission-line flux, with a measurable time delay (lag). When the continuum luminosity varies, the emission-line response follows with a measurable time lag (Cackett et al. 2021). The time lag τ corresponds to the average light-travel time between the photoionizing continuum source and the line-emitting regions. Assuming an idealized BLR consisting of spherically distributed clouds (Goad et al. 2012), then τ can be written as (Peterson 1997)

$$\tau = (1 + \cos\theta) \cdot \frac{R_{\mathrm{BLR}}}{c}, \tag{2.2}$$

Figure 2.4: Spherical BLR model and an isodelay surface, adopted from (Peterson & Horne 2004).

where R_{BLR} is the characteristic BLR radius, c is the speed of light, and θ is the angle between the line of sight and the position vector of the emitting gas with respect to the central source (see Figure 2.4) (Peterson 1997). The circle in Figure 2.4 represents the BLR modeled as spherical distribution of the clouds. For a fixed lag τ, the emitting regions that respond at that delay lie on a paraboloid aligned with the observer's line of sight, known as an isodelay surface. Therefore, emission observed at a given lag τ originates from the intersection of the BLR distribution with the corresponding isodelay surface (Peterson 1997). Thus, reverberation mapping can be used to "map" the BLR by inferring a characteristic BLR radius from the measured time lag (Peterson 1997). However, the observer receives emission from a range of delays (i.e., effectively from many isodelay surfaces), so the so-called transfer equation is required, which integrates over all delays (Peterson 1997):

$$L\left(t\right) = \int \Psi\left(\tau\right) C\left(t - \tau\right) d\tau. \tag{2.3}$$

Here, $\Psi(\tau)$ is the transfer function, which encodes the BLR geometry and kinematics, $C(t)$ is the continuum light curve, and $L(t)$ is the emission-line light curve (Peterson 1997). Although the BLR response is, in principle, fully described by the transfer function $\Psi(\tau)$, the lag is commonly estimated using cross-correlation techniques. In practice, recovering the full transfer function $\Psi\left(\tau\right)$ requires densely sampled, high signal-to-noise light curves spanning a duration much longer than the expected lag. Since real monitoring campaigns are often affected by observational gaps and noise, such reconstructions are rarely possible (Horne et al. 2004; Peterson 1993). For this reason, this project focuses on measuring the mean time lag between continuum and emission-line variations using the interpolated cross-correlation function (ICCF) method (Gaskell & Peterson 1987).

2.2.2 Lag Measurement

Using the notation of Peterson 1997, the cross-correlation function between the ionizing continuum and an emission line is defined as

$$F_{\mathrm{CCF}}(\tau) = \int_{-\infty}^{\infty} L(t)C(t - \tau)dt. \tag{2.4}$$

The auto-correlation function of the ionizing continuum is

$$F_{\mathrm{ACF}}(\tau) = \int_{-\infty}^{\infty} C(t)C(t - \tau)dt. \tag{2.5}$$

Together with the transfer equation (Equation 2.3), the cross-correlation function can be written as the convolution of the transfer function and the auto-correlation function of the ionizing continuum:

$$F_{\mathrm{CCF}}(\tau) = \int_{-\infty}^{\infty} \Psi(\tau')F_{\mathrm{ACF}}(\tau - \tau')d\tau'. \tag{2.6}$$

The lag is commonly defined as either the peak location (τ_{peak}) or the centroid (τ_{centroid}) of the CCF (Peterson 1997). While τ_{peak} is defined as the location of the CCF maximum, τ_{centroid} is calculated over all CCF points above a selected threshold, typically 80% of the peak value. Because the CCF is closely related to the transfer function, it is possible to infer a characteristic BLR size associated with the emission-line response (Peterson 1997), which can be expressed as

$$R_{\mathrm{BLR}} = c \cdot \tau_{\mathrm{centroid}}. \tag{2.7}$$

This follows from the light-travel timescale (Peterson et al. 2004). Since the centroid lag is generally considered a more robust estimator of the mean BLR light-travel time of the BLR (Peterson et al. 2004), it is used in this project.

The uncertainty of the measured lag is estimated using a Monte Carlo approach combining flux randomization (FR) and random subset selection (RSS) (Peterson et al. 1998; Peterson et al. 2004). In the FR step, each flux value is randomly perturbed according to its measurement uncertainty. In the RSS step, N data points are drawn randomly with replacement, while duplicate selections are discarded, resulting in a new light curve with $M \leq N$ points. For each realization, the ICCF analysis is repeated, yielding a distribution of centroid lags. The uncertainties are estimated from the distribution of centroid lags obtained from the simulations (Peterson et al.

2004). The 16th and 84th percentiles of this distribution are adopted as the bounds of the 1σ confidence interval (Peterson et al. 1998).

2.2.3 Black Hole Mass

The reverberation mapping method can be used not only to measure the characteristic size of the BLR, but also to estimate the mass of the central SMBH. Under the assumption that the gas dynamics in the BLR are dominated by the gravitational potential of the central SMBH, the black hole mass can be estimated using the virial theorem (Peterson et al. 2004).

The centroid time lag τ_{centroid} provides an estimate of the characteristic BLR radius via Equation 2.7. Together with the velocity dispersion ΔV of the BLR gas, the virial mass is given by

$$M_{\mathrm{vir}} = \frac{R_{\mathrm{BLR}}\,\Delta V^2}{G}. \tag{2.8}$$

The black hole mass is then given by

$$M_{\mathrm{BH}} = f \cdot M_{\mathrm{vir}}. \tag{2.9}$$

Here, G denotes the gravitational constant, and f is a scale factor that accounts for the unknown geometry, kinematics, and inclination of the BLR (Peterson et al. 2004).The velocity dispersion ΔV can be estimated from the widths of the broad emission lines (Peterson et al. 2004).

The scale factor f is calibrated by matching reverberation-based black hole masses to the empirical $M_{\mathrm{BH}} - \sigma_*$ relation observed in inactive galaxies, where σ_* denotes the stellar velocity dispersion of the galactic bulge (Onken et al. 2004). Different studies have reported values of f based on various AGN samples, for example, $f = 5.5$ (Onken et al. 2004), $f = 4.31$ (Grier et al. 2013), and $f = 3.6$ (Graham et al. 2011). The calibration of the scale factor also depends on the measurement method used for the line width of the broad emission lines (Peterson et al. 2004). Two commonly used measures are the line dispersion σ_{line} (see (Peterson et al. 2004)) and the FWHM. As this work focuses on the FWHM measures and the previously named scale factories where estimated with the line dispersion measure, a average scale factor of $f = 1.8$ gets adopted, following Probst et al. 2025. This value bases on the average scale factor $f = 3.6$ reported by Graham et al. 2011 and takes the relation $\mathrm{FWHM}/\sigma_{\mathrm{line}} \approx 2$ Peterson et al. 2004 into account.

2.3 Bowen Fluorescence of OIλ8446

Previous studies of NGC 4593 report strong emission in the low-ionization lines O I λ8446 and the Ca II λ8498 λ8542 λ8662 triplet (Ochmann et al. 2025). In particular, O I λ8446 is of interest because it can be enhanced through a fluorescence mechanism referred to as Bowen fluorescence (Grandi 1980). The mechanism was first described by I.S. Bowen in 1934 to explain unexpected emission lines in nebular spectra. This mechanism describes a resonant line-pumping process in which photons emitted by one ion are absorbed by another ion of a different species via a permitted transition enabled by a near coincidence in wavelength between the pumping line and the absorbing transition. The resulting de-excitation leads to an enhancement of the emission lines (Bowen 1934).

One transition that can be enhanced by Bowen fluorescence is O I λ8446, which can be pumped by Lyβ photons (Netzer & Penston 1976). In this process, Lyβ photons at λ1025.72 Å are absorbed by neutral oxygen through the near-resonant transition $2p^4\,^3P_2 \rightarrow 3d\,^3D^0$ of O I at λ1025.77 Å. The excited $3d\,^3D^0$ level decays to $3p\,^3P$, which then decays to $3s\,^3S°$, emitting the O I λ8446 emission line (see figure 2.5) (Grandi 1980). This provides an additional excitation channel for O I λ8446, in addition to recombination.

Figure 2.5: Energy level diagram displaying the process of Bowen fluorescence pumping of OI, adopted from (Grandi 1980).

3. Campaign and Data Preparation

The analysis of this campaign is based on the observation campaign of NGC4593 in 2016 by Cackett et al. 2018. This campaign took place between the 12th of July and the 6th of August with daily observations, which resulted in 26 successful out of 27 observations. It was performed with the Hubble Space Telescope (HST) using the Space Telescope Imaging Spectrograph (STIS) with the three different Gratings. The following section will cover an overview of the properties and specifications of NGC4593 and the campaign in 2016.

3.1   NGC4593

NGC 4593 is classified as a Seyfert 1 galaxy with a barred spiral morphology of type (R)SB(rs)b (Denney et al. 2006). It is located at RA $= 12^{\text{h}}39^{\text{m}}39.44^{\text{s}}$, Dec $= -05°20'39.03''$ (J2000) and has a redshift of $z = 0.0083 \pm 0.0005$, corresponding to a distance of $\sim 35.9\,\text{Mpc}$ (Koss et al. 2022) assuming a ΛCDM cosmology. The galaxy exhibits a prominent large-scale bar and nuclear dust ring connected to dust lanes along the bar, as seen in Figure 3.1.

The AGN in NGC 4593 exhibits strong broad emission lines, including Balmer and Lyman lines as well as He, O, and Ca lines among others (Kollatschny & Dietrich 1997; Cackett et al. 2018; Ochmann et al. 2025). Several variability and reverberation-mapping campaigns have monitored different broad emission lines, including Kollatschny & Dietrich 1997; Denney et al. 2006. They reported FWHM values from the mean (AVG) and root-mean-square (RMS) spectra of their respective campaigns. The RMS spectrum is defined as the standard deviation of the flux at each wavelength across epochs:

$$F_{\text{RMS}}(\lambda) = \sqrt{\frac{1}{N-1}\sum_{i=1}^{N}\left[F_i(\lambda) - \bar{F}(\lambda)\right]^2}, \qquad (3.1)$$

Figure 3.1: Screenshot of NGC 4593 visualized with Aladin Lite (*Aladin Lite* 2025) using DSS2 survey imagery (STScI 2025). The image is oriented with north up and east to the left. Right ascension increases to the left and declination increases upward.

with the mean spectrum at wavelength λ given by

$$\bar{F}(\lambda) = \frac{1}{N} \sum_{i=1}^{N} F_i(\lambda) \,. \tag{3.2}$$

Kollatschny & Dietrich 1997 measured $\mathrm{FWHM}_{\mathrm{AVG/RMS}} = (3400 \pm 200)\,\mathrm{km\,s}^{-1}$ for Hα, while Denney et al. 2006 reported for Hβ $\mathrm{FWHM}_{\mathrm{AVG}} = (5142 \pm 16)\,\mathrm{km\,s}^{-1}$ and $\mathrm{FWHM}_{\mathrm{RMS}} = (4141 \pm 416)\,\mathrm{km\,s}^{-1}$. Based on these broad-line widths, they estimated the SMBH mass to be $M \approx 1.4 \times 10^7\,M_\odot$ (Kollatschny & Dietrich 1997) and $M = (9.8 \pm 2.1) \times 10^6\,M_\odot$ (Denney et al. 2006). Overall, these results suggest that the SMBH mass is of order $10^7\,M_\odot$.

Furthermore, NGC 4593 shows a rare double-peaked emission-line complex involving O I $\lambda 8446$ and the Ca II $\lambda 8498$, $\lambda 8542$, $\lambda 8662$ triplet (Ochmann et al. 2025). Ochmann et al. 2025 found that the Ca II triplet has an intensity ratio of 1:1:1 and line profiles that closely resemble those of O I $\lambda 8446$, exhibiting a red-to-blue peak ratio of 4:3 and a FWHM of $\approx 3700\,\mathrm{km\,s}^{-1}$, suggesting that these lines originate in a similar high-density emission region. A fit of the asymmetric line profile of Ca II $\lambda 8662$ with an elliptic accretion disk model, shows a eccentric of $e \approx 0.22$ and a low-inclination of $i \approx 11°$ Ochmann et al. 2024.

3.2 The 2016 Hst Campaign

The campaign of Cackett et al. 2018 was designed to study wavelength-dependent continuum lags. It took place between the 12th of July and the 6th of August with daily observations, which resulted in 26 successful out of 27 observations. Observa-

tions were carried out with the Hubble Space Telescope (HST) using the Space Telescope Imaging Spectrograph (STIS) and three different gratings. The low-resolution STIS gratings provided continuous spectral coverage over a broad wavelength range. In each observation, spectra were obtained using the G140L, G430L, and G750L. All spectra were acquired with the $52'' \times 0.2''$ slit.

The characteristics of the STIS gratings used in this work are summarized in Table 3.1. After standard pipeline processing, charge-transfer inefficiency (CTI) corrections were applied using an algorithm based on (Anderson & Bedin 2010). Remaining hot pixels were removed manually by interpolating the flux from neighboring pixels.

Table 3.1: Overview of STIS grating characteristics (Institute 2025).

Grating	Range [Å]	Exp. Time [s]	Res. Power	Dispersion [Å/pixel]
G140L	1119–1715	1234	~ 1000	0.6
G430L	2888–5697	298	$\sim 500 - 1000$	2.73
G750L	5245–10233	288	$\sim 500 - 1000$	4.92

3.3 Intercalibration and Determination of AVG and RMS Spectra

Reverberation mapping requires multiple epochs to capture variability. For the 2016 campaign of NGC 4593, we retrieved 27 spectra from the *Hubble Advanced Spectral Products (HASP)* 2025 archive using the HASP search form in *Mikulski Archive for Space Telescopes (MAST)* 2025 . 26 of these spectra are usable for further analysis. The top panel of Figure 3.2 shows all spectra in the spectral range from 4000Å to 9000Å.

For the subsequent analysis, the average spectrum (AVG) is obtained by averaging over all epochs, improving the signal-to-noise ratio (S/N). Furthermore it is essential for the reverberation mapping analysis to identify variability between the epochs, which can be assessed with the root-mean-spuare (RMS) spectrum, defined as the standard deviation of the flux at each wavelength across epochs (see. Equation 3.1). Constant features, such as narrow emission lines, vanish in the RMS spectrum, leaving only variable components such as broad emission lines. The top panel of Figure 3.2 shows the AVG and RMS spectra from the original retrieved data. Residual variability is still noticeable in nominally non-varying lines, particularly in the forbidden line [O III] $\lambda5007$. This indicates small wavelength misalignment between epochs.

Therefore, an intercalibration anchored to the narrow [O III] $\lambda5007$ line was performed. This was achieved by shifting the wavelengths of the individual spectra and scaling the line flux to a constant value. As a narrow line, the flux of [O III] $\lambda5007$ can be assumed to remain constant over the timescale of the campaign. Based on this assumption, the flux of each spectrum was scaled to $(106 \pm 5) \times 10^{-15} \, \mathrm{erg \, s^{-1} \, cm^{-2}}$ and the wavelength was shifted by a maximum of 1Å.

Figures 3.2 shows a comparison of the original and the intercalibrated epochs and the corresponding AVG and RMS spectra. The disappearance of narrow features in the calibrated RMS spectrum, especially the [O III] $\lambda5007$ line, confirms that the apparent variability in the RMS of the original epochs was induced by the wavelength shifts between them, rather than intrinsic line variability. However the intercalibration was only applied to the optical part of the spectra due to its limited reliability. In the following analysis, the intercalibrated AVG and RMS spectra are used for the optical range obtained with the G430L and G750L gratings, while the AVG and RMS spectra from the original epochs are used for the UV emission-line analysis, as these were acquired with the G140L grating.

Figure 3.2: Comparison of the spectral range between 4000Å and 9000Å from the 2016 HST campaign of NGC 4593, showing the effects of [O III] λ5007 intercalibration on both the individual spectra (top) and the derived average and rms spectra (bottom).

4. Reverberation Mapping Analysis of NGC4593

4.1   Line Identification

To begin the RM analysis, the emission lines in the AVG spectrum are identified. This is done for the optical–NIR range $3900\,\text{Å}$–$9000\,\text{Å}$ and for the UV range $1100\,\text{Å}$–$1700\,\text{Å}$.

In the optical–NIR range (see Figure 4.1), several prominent broad emission lines are identified: Balmer lines from $H\alpha$ – $H\epsilon$; He I $\lambda4471$, He I $\lambda5016$, He I $\lambda5876$ and He I $\lambda7065$; the He II line He II $\lambda4686$; and the low-ionization lines O I $\lambda8446$ and the Ca II $\lambda8498\,\lambda8542\,\lambda8662$ triplet. All of these lines show variability in the RMS spectrum. For the subsequent analysis, the Balmer lines $H\alpha$ – $H\delta$, He II $\lambda4686$ and He I $\lambda5876$ are selected for the subsequent analysis, as they show the most pronounced variation in the RMS spectrum. Because the low-ionization line O I $\lambda8446$ has rarely been included in RM studies and shows small but noticeable variability, it is included as well. Two prominent Fe II emission line bands are also present in the optical spectrum as well, one between $\sim 4489\,\text{Å} - 4629\,\text{Å}$, blending with He I $\lambda4471$ and He II $\lambda4686$, and another between $\sim 5169\,\text{Å} - 5336\,\text{Å}$. The AVG spectrum also shows several narrow forbidden emission lines, with [O III] $\lambda4363$, $\lambda4959$, and $\lambda5007$ being the most prominent. As they are assumed to be constant over the timescale of the campaign, they show no significant variability in the RMS spectrum.

In the UV spectrum (Figure 4.2), five broad emission lines are identified, which will also be included in the subsequent analysis: $Ly\alpha$, which overlaps with the N V $\lambda\lambda1238$, 1242 doublet; Si IV $\lambda\lambda1393$, 1402; C IV $\lambda\lambda1548$, 1550; and He II $\lambda1640$. $Ly\alpha$ and C IV $\lambda\lambda1548$, 1550 show strong variability, whereas N V $\lambda\lambda1238$, 1242 and He II $\lambda1640$ vary more weakly but remain detectable. In the RMS spectrum, the variation of N V $\lambda\lambda1238$, 1242 is overlapping with $Ly\alpha$ emission, but is still distinguishable. Similarly, the He II, $\lambda1640$ variability overlaps with the semi-forbidden O III] $\lambda\lambda1660$, 1666 doublet.

Figure 4.1: Optical-to-NIR AVG and RMS spectrum with identified emission lines.
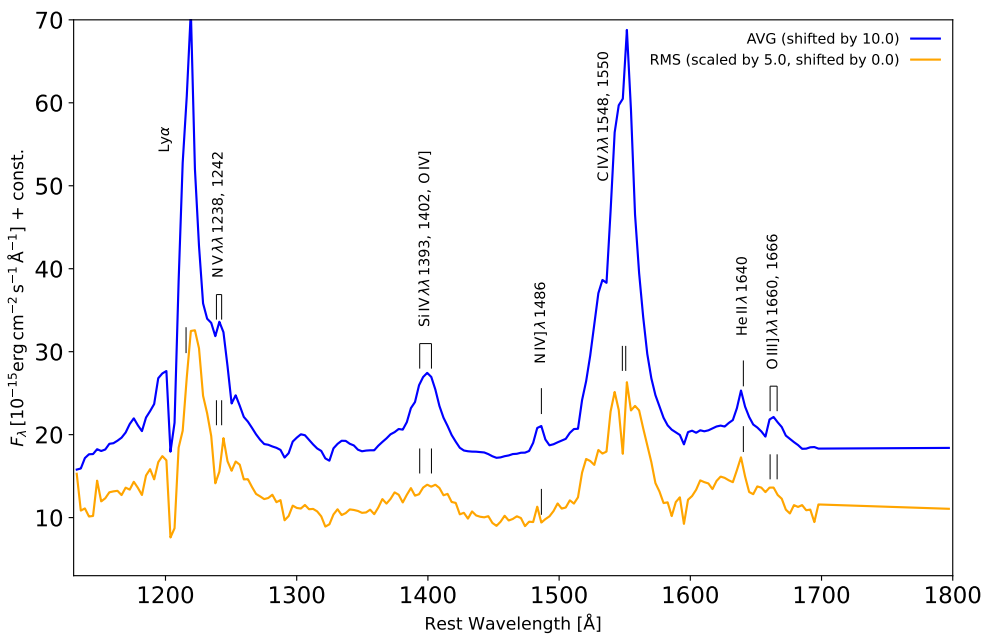
Figure 4.2: UV spectrum AVG and RMS spectrum with identified emission lines

4.2 Emission Line and Continua Measurement

After identifying and selecting suitable emission lines for the subsequent analysis, their fluxes and light curves are measured. This is performed using a Python-based tool called GECHO, developed by M. Probst. This tool is able to import full campaigns, determine AVG and RMS spectra, extracting lightcurves and conduct further measurements, naming here line-width measurements and lags measurement based on the methods of Gaskell & Peterson 1987 and Peterson et al. 2004. These methods are discussed further in Sections 4.4 and 4.5.

The extraction of the light curves with GECHO follows the same principle as in previous RM campaigns (e.g. Kollatschny & Dietrich 1997; Probst et al. 2025). Figure 4.3 shows the GECHO graphical user interface (GUI), which provides a side-by-side view of the campaign's AVG and RMS spectra. The line flux at each epoch is obtained by integrating the flux density over the wavelength range, marked in red in Figure 4.3. The integration boundaries are chosen to include the variable part of the emission line while excluding contributions from neighboring lines. To account for the surrounding continuum, a linear pseudo-continuum is estimated from two line-free wavelength windows on the blue and red side of the emission line, shown in grey in Figure 4.3. The adopted integration limits and pseudo-continua for each line are listed in Table 4.1.
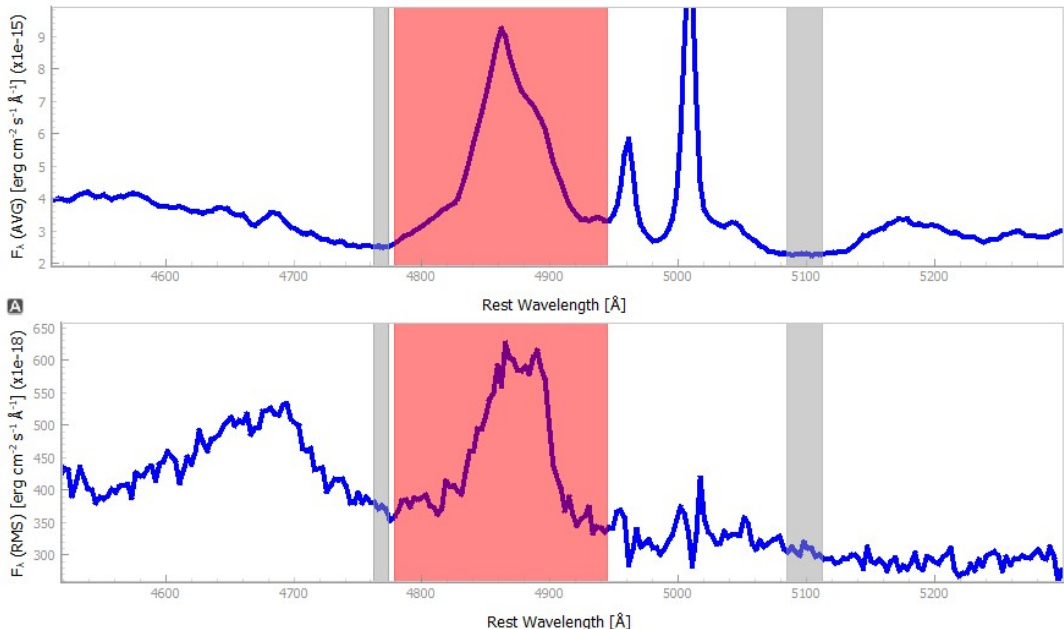
Figure 4.3: Screenshot of the GECHO graphical user interface (GUI). Shown is an example of the selection of the integration boundaries for Hβ and corresponding blue and red pseudo-continuum used to measure the integrated line flux.

In addition to the emission line light curves, continuum light curves are also extracted to serve as a proxy for the variable ionizing continuum. The continuum windows are adopted from (Cackett et al. 2018), and their light curves are extracted with GECHO. The wavelength range for the continua are listed in Table 4.2.

Table 4.1: Integration Limits and Pseudo-Continua range of the measured emission lines

Line	Integration Limits [Å]	Pseudo-Continua [Å]
Lyα	$1207 - 1238$	$1151 - 1161, 1461 - 1469$
Nv $\lambda\lambda$1238, 1242	$1207 - 1238$	$1151 - 1161, 1461 - 1468$
Si$\textsc{iv}$ $\lambda\lambda$1393, 1402	$1358 - 1423$	$1151 - 1161, 1461 - 1469$
C$\textsc{iv}$ $\lambda\lambda$1548, 1550	$1511 - 1578$	$1461 - 1469, 1680 - 1685$
Hα	$6453 - 6695$	$6107 - 6129, 6861 - 6900$
Hβ	$4779 - 4944$	$4762 - 4774, 5085 - 5112$
Hγ	$4230 - 4427$	$4197 - 4220, 4435 - 4450$
He$\textsc{i}$ λ5875	$5742 - 6039$	$5645 - 5653, 6044 - 6057$
He$\textsc{ii}$ λ1640	$1599 - 1645$	$1461 - 1468, 1680 - 1685$
He$\textsc{ii}$ λ4685	$4545 - 4758$	$4435 - 4450, 4762 - 4774$
O$\textsc{i}$ λ8446	$8380 - 8498$	$8005 - 8031, 8850 - 8955$
O$\textsc{iii}$ λ5007	$4982 - 5033$	$4762 - 4774, 5085 - 5112$

Table 4.2: Wavelength range of the measured continua

Line	Integration Limits [Å]
Cont. 1150	$1151 - 1161$
Cont. 4010	$4026 - 4033$
Cont. 4440	$4435 - 4450$
Cont. 5100	$5085 - 5112$
Cont. 6110	$6107 - 6129$
Cont. 6880	$6861 - 6900$
Cont. 8015	$8005 - 8031$
Cont. 8900	$8864 - 8955$

4.2.1 Variability Statistics

To quantify the variability of the emission lines and continua variability statistics the definition by Rodriguez-Pascual et al. 1997 are adopted. They name the maximum-to-minimum flux ratio R_{max} and the fractional variability F_{var} as two common measures of variability. R_{max} is defined as the ratio of the the extreme of the integrated fluxes, F_{min} and F_{max}, and F_{var} as:

$$F_{\mathrm{var}} = \frac{\sqrt{\sigma_F^2 - \Delta^2}}{\langle F \rangle} \tag{4.1}$$

29

Here, σ_F^2 denotes the standard deviation, $\langle F \rangle$ the mean flux and Δ^2 the mean square value of the flux uncertainties, which is defined by:

$$\Delta^2 = \frac{1}{N} \sum_{i=1}^{N} \Delta_i^2 \qquad (4.2)$$

The results for all parameters can be found in the Tables 4.3.

First, considering R_{max} and F_{var} of the continuum lightcurves, all measured continua show similar variability, except for the UV continuum around 1150 Å, which shows significantly higher variability with $R_{\mathrm{max}} = 2.58$ and $F_{\mathrm{var}} = 0.28$ than the optical and NIR continua. These continua show a fairly uniform variation between $R_{\mathrm{max}} \simeq 1.33 - 1.59$ and $F_{\mathrm{var}} \simeq 0.08 - 0.14$.

The lightcurves of the Balmer emission lines exhibit lower variability, which increases towards the higher-order Balmer lines, with values between $R_{\mathrm{max}} \simeq 1.15 - 1.52$ and $F_{\mathrm{var}} \simeq 0.03 - 0.1$. The helium lightcurves show a similar variability to Hδ with values between $R_{\mathrm{max}} \simeq 1.48 - 1.62$ and $F_{\mathrm{var}} \simeq 0.09 - 0.11$ and the OI $\lambda 8446$ a similar variability to the Balmer lines with $R_{\mathrm{max}} \simeq 1.22$ and $F_{\mathrm{var}} \simeq 0.04$.

The variability of the emission line lightcurves in the UV region is on a similar level as that of the helium light curves in the optical region, with $R_{\mathrm{max}} \simeq 1.42 - 1.62$ and $F_{\mathrm{var}} \simeq 0.14$, with the exception of the He II, $\lambda 1640$ lightcurve, which shows significant higher variability with $R_{\mathrm{max}} \simeq 3.12$ and $F_{\mathrm{var}} \simeq 0.31$.

4.2.2 Uncertainties Estimation

The uncertainties of the continuum and emission-line light curves are estimated based on the spectral noise and a systematic uncertainty introduced by the inter-calibration.

For the continuum light curves, the per-epoch noise is estimated as

$$\sigma_i^{\mathrm{cont}} = \frac{\sigma_{f_i}}{\sqrt{N}}, \qquad (4.3)$$

where σ_{f_i} denotes the standard deviation of the flux density within the selected continuum window in epoch i, and N is the number of pixels within that window. For the emission-line light curves, the noise is estimated from the scatter in the interpolated pseudo-continuum, $\sigma_i^{\mathrm{noise}}$, as

$$\sigma_i^{\mathrm{line}} = \frac{\sigma_i^{\mathrm{p.cont.}} \Delta\lambda}{\sqrt{N}}, \qquad (4.4)$$

where $\Delta\lambda$ denotes the integration range of the emission line and N is the number of pixels across the integration window.

As each epoch has been scaled to the flux of the narrow [O,III] $\lambda5007$ line after the intercalibration, the systematic uncertainty introduced by the intercalibration is estimated from its fractional variability, $F_{\mathrm{var}}^{[\mathrm{O\,III}]\,\lambda5007}$. The total uncertainty of the measured flux at epoch i, f_i, is then

$$\sigma_i = \sqrt{\left(\sigma_i^{\mathrm{cal.}}\right)^2 + \left(\sigma_{\mathrm{noise},i}\right)^2}, \tag{4.5}$$

with

$$\sigma_i^{\mathrm{cal.}} = F_{\mathrm{var}}^{[\mathrm{O\,III}]\,\lambda5007} f_i. \tag{4.6}$$

Here, $\sigma_{\mathrm{noise},i}$ corresponds to σ_i^{cont} for continuum light curves or to σ_i^{line} for emission-line light curves.

Table 4.3: Variability statistics of the measured continua and emission lines with minimum flux F_{min} and maximum flux density or integrated flux F_{max}, peak-to-peak ratio R_{max}, mean $\langle F \rangle$, standard deviation σ_F and fractional variation F_{var}.

Continuum/Line	F_{min}	F_{max}	R_{max}	$\langle F \rangle$	σ_F	F_{var}
Cont. 1150	0.52	1.35	2.58	0.86	0.25	0.28
Cont. 4010	2.68	4.21	1.57	3.49	0.47	0.14
Cont. 4440	2.42	3.73	1.54	3.14	0.39	0.12
Cont. 5600	1.36	2.15	1.59	1.82	0.25	0.14
Cont. 6110	1.49	2.27	1.53	1.9	0.23	0.12
Cont. 6880	1.33	2.01	1.5	1.72	0.2	0.11
Cont. 8015	1.18	1.69	1.43	1.48	0.15	0.1
Cont. 8900	1.14	1.52	1.33	1.38	0.11	0.08
Hα	130.83	149.85	1.15	141.35	4.83	0.03
Hβ	38.29	45.4	1.19	42.32	1.94	0.05
Hγ	18.82	24.38	1.3	21.91	1.29	0.06
Hδ	7.17	10.92	1.52	9.13	0.94	0.1
He II $\lambda4685$	11.93	17.7	1.48	14.82	1.6	0.11
He I $\lambda5875$	8.53	13.82	1.62	11.58	1.01	0.09
O I $\lambda8446$	7.47	9.13	1.22	8.32	0.37	0.04
Lyα	66.87	94.88	1.42	82.21	8.03	0.1
Si IV $\lambda\lambda1393, 1402$	21.93	35.5	1.62	27.92	3.88	0.14
C IV $\lambda\lambda1548, 1550$	115.31	165.57	1.44	138.77	12.12	0.09
He II $\lambda1640$	6.83	21.29	3.12	13.29	4.13	0.31
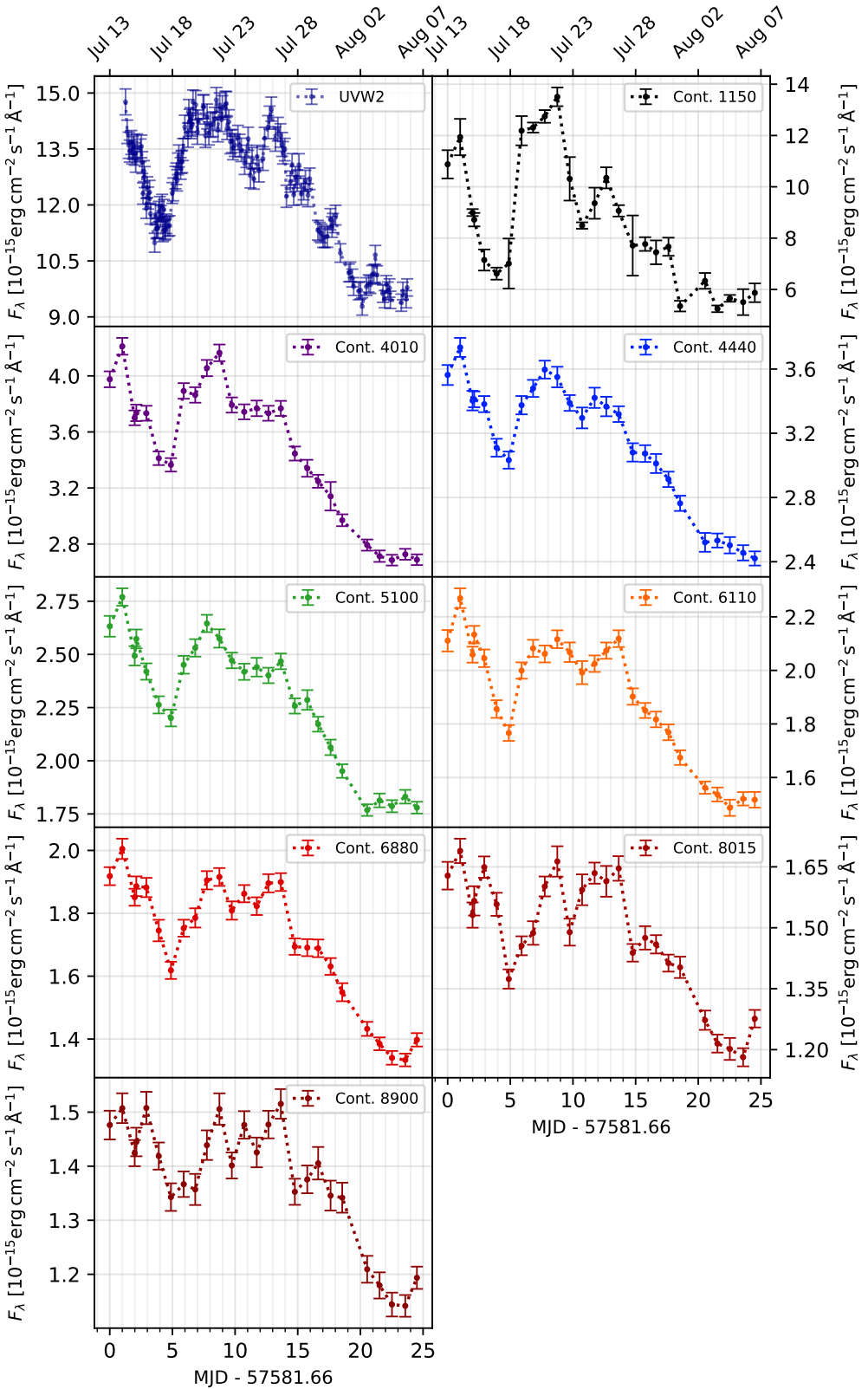
Figure 4.4: Comparison of the continua lightcurves. The first panel shows the UVW2 continuum lightcurve obtained from McHardy et al. 2018, while the other panels show the measured continua defined in Table 4.2
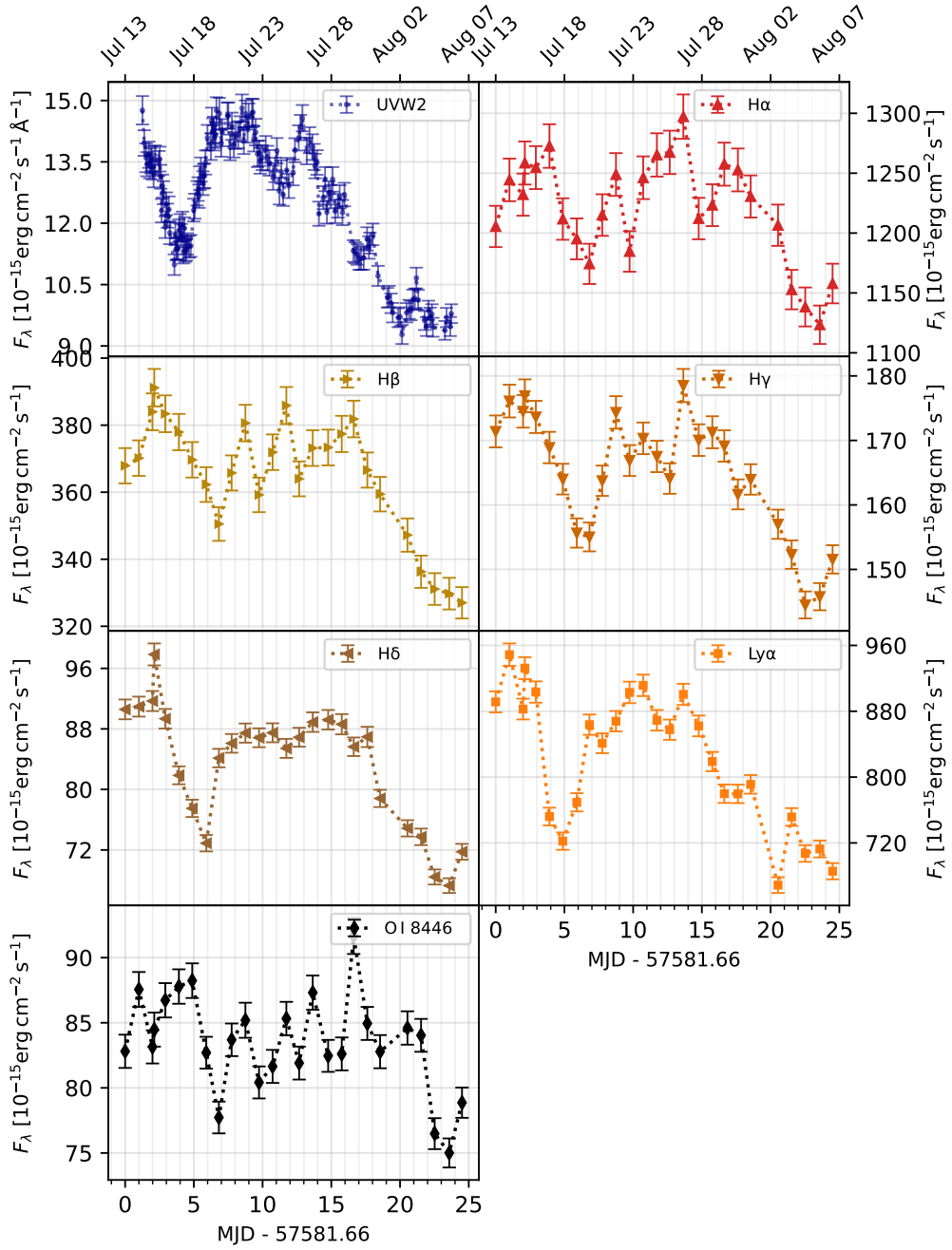
Figure 4.5: Comparison of the Balmer-line, Lyα, and O,I, $\lambda 8446$ light curves with the UVW2 reference light curve in the first panel. The UVW2 light curve is adopted from McHardy et al. 2018.

33
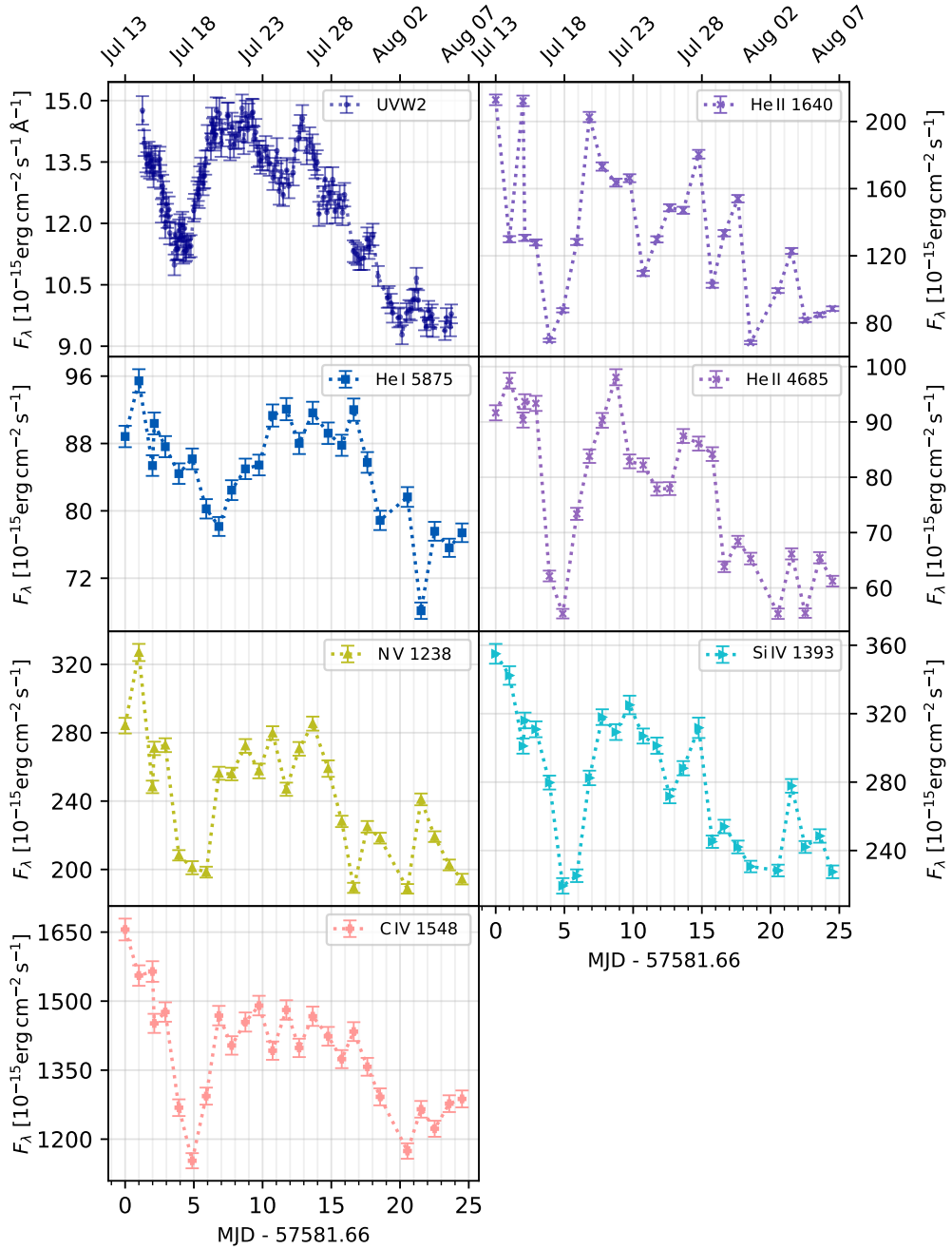
Figure 4.6: Comparison of the Helium and UV light curves with the UVW2 reference light curve in the first panel. The UVW2 light curve is adopted from McHardy et al. 2018.

4.3   Lightcurves

The extracted continuum and emission-line light curves are shown in Figures 4.4, 4.5, and 4.6. In addition to the extracted HST light curves, the UVOT UVW2 lightcurve is included in the subsequent analysis, which was taken with *Swift* by McHardy et al. 2018 and has also been used in Cackett et al. 2018. IT showes a higher sample size and was taken during nearly every orbit for 6.4 d between July 13 and July 18, 2016 (McHardy et al. 2018). The central wavelength of the UVW2 lightcurve is located at about 1930 Å (McHardy et al. 2018).

When compared, all continuum light curves show a broadly similar shape (see Figure 4.4). The light curves start at high flux and then decrease by about 50–80% relative to their maxima within the first 1–4 days, reaching a minimum between days 4 and 5. Afterwards, the flux increases again in all light curves. The UV continua show a plateau-like behavior from days 6 to 9, followed by a smaller decline between days 9 and 13, before rising again to a peak around day 13. A similar pattern is also noticeable in the other continuum light curves, but becomes less clear at higher wavelengths. While the optical continua also show higher flux levels between days 6 and 9 than between days 9 and 13, the near-IR continua display a more scattered plateau over this interval. Towards the end of the campaign, the flux decreases again towards a minimum, with smaller short-term fluctuations, followed by a slight rise in the final days of the campaign in the UV and NIR bands.

The estimation of the physical distance between the SMBH and the region from which the emission lines originate is the main goal of this RM analysis. Assuming that the continuum radiation originates from the accretion disk, it is common to use the bluest available continuum as reference for the time lag estimation, which is expected to originate closest to the SMBH (Ochmann et al. 2026). In this analysis, this would be the continuum around 1150 Å. Nevertheless, the UVW2 continuum was selected as the main reference lightcurve for the subsequent analysis due to its higher sampling rate. To accommodate this, the delay between the UV continuum light curve around 1150 Å and the UVW2 light curve has to be taken into account. Figures 4.5 and 4.6 show the lightcurves of the measured broad emission lines in the optical-to-NIR range and in the UV range respectively. Overall, similarities to the shape of the UVW2 lightcurve are noticeable: A strong decrease in flux, followed by a central part with higher flux and a decrease towards the end of the campaign. The main exceptions are the O I λ8446 and He II λ1640 lightcurves, which are much more scattered than the others. Here, it has to be noted, that the integration boundaries of He II λ1640 did not include parts of its red flank, as it is blended with the semi-

forbidden emission line doublet O III] $\lambda\lambda$1660, 1666. Nevertheless, it is possible to notice a pronounced minimum similar to that in the UVW2 light curve in these curves.

By comparing these features, a shift of a few days between the light curves is already apparent. The flux minima of the Balmer lines, O I λ8446, and He I λ5875 occur between days 6 and 7, whereas the minima of the He II light curves and the UV emission lines Lyα, Si IV $\lambda\lambda$1393, 1402, and C IV $\lambda\lambda$1548, 1550 occur between days 4 and 5. This provides a first estimate of a time lag of about 2–3 days for the first group of emission lines and about 0–1 days for the second group. A more detailed investigation of the time lags is presented in Section 4.5.

4.4 Line Profiles

By analyzing the shape and line width of the emission line profiles it is possible to draw conclusions about the kinematics of their emitting region. Equally to the lightcurve extraction, a correction of the underlying continuum is necessary to enable comparison between the extracted profiles. Following the same procedure done for the lightcurves, an underlying linear continuum is interpolated, using line-free wavelength widows on the blue and red side for each emission line in both the AVG and RMS spectra. The selected boundaries of the pseudo-continua are listed in Table 4.4. By subtracting this interpolated continuum, a new zero-flux baseline for each line profile gets defined. Subsequently, the line profile is converted to velocity space using the relativistic Doppler equation

$$v_i = c \cdot \frac{\lambda_i^2 - \lambda_{\text{central}}^2}{\lambda_i^2 + \lambda_{\text{central}}^2}. \tag{4.7}$$

Here, λ_i denotes the wavelength values, λ_{central} the central wavelength of the emission line in rest-frame and c the speed of light. Finally, the flux is getting normalized to the maximum of each line profile. Figure 4.7 shows an overview of the extracted and normalized line profiles. For the doublet the rest-frame wavelength of the second line gets used as the central wavelength of the emission line.

4.4.1 FWHM

The height of the line profile is defined between its maximum and the zero-flux baseline. For line profiles which show clearly distinguishable flanks without overlapping profiles of neighboring lines, the measurement of their FWHM is performed

36
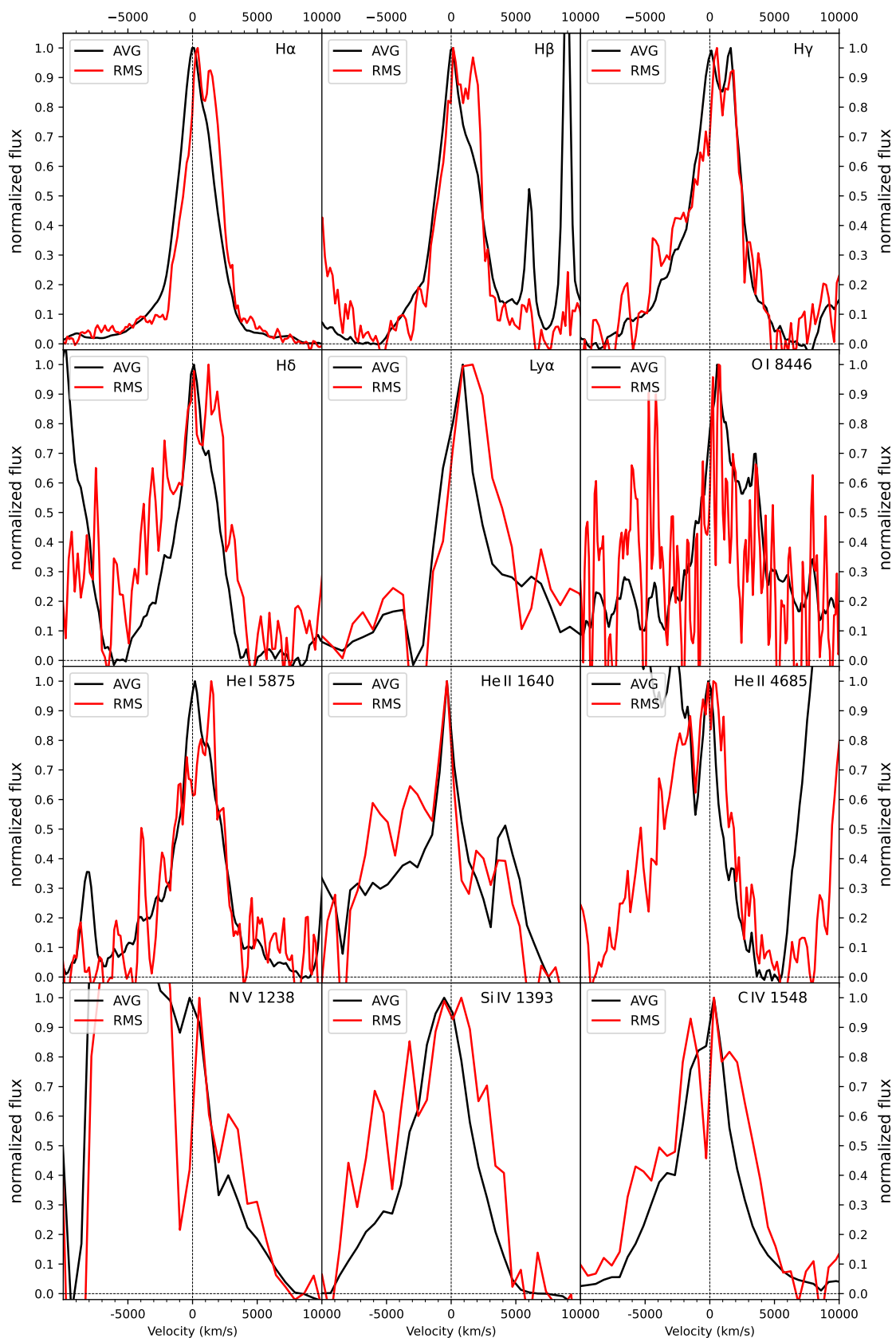
Figure 4.7: Normalized line profiles in the AVG and RMS spectra

Table 4.4: Boundaries of the blue and red pseudo-continua used for the interpolation of underlying continua for line profile extraction.

Line	Pseudo-Continua (avg) [Å]	Pseudo-Continua (rms) [Å]
Hα	$6194 - 6216, 6861 - 6900$	$6279 - 6301, 6742 - 6781$
Hβ	$4762 - 4774, 5085 - 5112$	$4762 - 4774, 4967 - 4984$
Hγ	$4197 - 4220, 4435 - 4450$	$4197 - 4220, 4417 - 4429$
Hδ	$4026 - 4033, 4197 - 4221$	$4006 - 4016, 4197 - 4211$
O I λ8446	$7999 - 8025, 8775 - 8798$	$8222 - 8238, 8748 - 8767$
He I λ5875	$5679 - 5697, 6044 - 6057$	$5736 - 5753, 6027 - 6045$
He II λ1640	$1461 - 1468, 1679 - 1685$	$1461 - 1468, 1679 - 1685$
He II λ4685	$4198 - 4225, 4762 - 4774$	$4543 - 4554, 4766 - 4778$
Lyα	$1151 - 1161, 1270 - 1285$	$1151 - 1161, 1340 - 1355$
N V $\lambda\lambda$1283, 1242	$1151 - 1161, 1270 - 1285$	$1151 - 1161, 1340 - 1355$
Si IV $\lambda\lambda$1393, 1402	$1350 - 1360, 1430 - 1440$	$1340 - 1355, 1430 - 1440$
C IV $\lambda\lambda$1548, 1550	$1461 - 1468, 1679 - 1685$	$1461 - 1468, 1679 - 1685$

with GECHO. This is done by linear interpolation between the two intersections of the line profile at the height 0.5. If no data point is found at exactly 0.5, the two neighboring points are used to linearly interpolate the velocity at the cross-section of at 0.5.

The line profiles of Lyα, the Balmer lines, He I λ5875, C IV $\lambda\lambda$1548, 1550, Si IV $\lambda\lambda$1238, 1242 and He II λ1640 show a distinguishable line profile at half height in both their AVG and RMS spectra. For the line profile of He II λ4685 this only applies to its RMS profile, as its blue flank of its AVG profile is blended by the Fe II band between 4489 Å and 4629 Å. The FWHM measurement for the previous named emission lines are therefore performed with GECHO.

For the profiles, that are partly blended with neighboring line emission, the FWHM gets estimated, by doubling the width of the distinguishable flank of the profile in relation to the zero-velocity line. This is done for the AVG profile of He II λ4685, using its red flank as reference. The same approach is used for the N V $\lambda\lambda$1238, 1242 doublet in both AVG and RMS spectra, as it is blended with the Lyα profile.

The FWHM measurements for O I λ8446 is excluded from the subsequent analysis. Its AVG profile is blended with the Ca II λ8498, λ8542, λ8662 triplet, which makes it difficult to decompose. Although it was shown in Ochmann et al. 2025, that O I λ8446 in NGC4593 shows a similar shape that the as the Ca lines, it was not attempted in this work. In addition to that, the RMS profile shows very strong noise. While variability is noticeable, a clear profile is not distinguishable from the surrounding spectrum. The resulting FWHM values are listed in Table 4.5.

It has to be noted, that the line profiles of the AVG spectrum can also includes narrow components of the respective emission line (Peterson 1997), as well in some

cases a overlapping profile of a close narrow emission line (e.g. the [O III] λ4363 next to Hγ). The narrow components are hard to isolate in the profiles, which is why no attempt was made to decompose the AVG profiles. Having no narrow components in the RMS profiles, their FWHM will be used in subsequent analysis to describe the velocity dispersion of their emitting region.

The uncertainties are estimated based on the instrumental dispersion of the gratings (see Table 3.1), the shape of the line profiles (see Figure 4.7). Hα and He I λ5875 are measured with the G750L grating with a dispersion of 4.97 (Å/pixel); Hβ, Hγ, Hδ, and He II λ4685 are measured with the G430L grating with a dispersion of 2.73 (Å/pixel); and the UV emission lines are measured with the G140L grating with a dispersion of 0.6 (Å/pixel). By using Equation 4.7, this transforms to an equivalent dispersion per pixel in velocity space, listed in Table A.1. This dispersion is used as a minimum estimate for the uncertainty estimation.

The FWHM uncertainties of the RMS profiles of Hγ, He I λ5875, and the He II lines are scaled up due to their profile shape and noise. The RMS profile of Hδ it is much more scattered and extended at his blue flank at half height, which is why its uncertainty is estimated significantly higher. Same is done for the FWHM of Lyα, as it is blended with absorption in its blue flank and with the N IV $\lambda\lambda$1238, 1242 doublet in its red flank. The FWHM uncertainties for the profiles of the three doublets are estimated higher as well, due to their shape and superposition of their broad components. Finally, the uncertainties for the AVG and RMS profiles of N V $\lambda\lambda$1238, 1242 and for the AVG profile of He II λ4685 are set significantly higher, since they are estimated based on the width of only one profile flank.

Table 4.5: Measured FWHM and of the AVG and RMS line profiles.

Line	FWHM (avg)[km/s]	FWHM (rms)[km/s]
Lyα	3819 ± 350	4566 ± 350
Hα	2974 ± 250	3111 ± 250
Hβ	3439 ± 200	3437 ± 200
Hγ	4067 ± 200	3852 ± 400
Hδ	3398 ± 250	5905 ± 1000
He I λ5875	3477 ± 300	3952 ± 400
He II λ1640	2847 ± 500	6891 ± 600
He II λ4685	1839 ± 600	5971 ± 400
N V $\lambda\lambda$1238, 1242	3216 ± 800	3383 ± 1000
Si IV $\lambda\lambda$1238, 1242	5184 ± 500	10005 ± 1000
C IV $\lambda\lambda$1548, 1550	5413 ± 500	8428 ± 500

4.4.2 Balmer Line-Profiles

Looking at the comparison of the Balmenr RMS profiles in Figure 4.8, they all show a overall similar shape. The center of the profiles is shifted to positive velocities, with the peaks located between ~ 0–$500\,\mathrm{km\,s^{-1}}$ and between ~ 1500–$2000\,\mathrm{km\,s^{-1}}$. Both peaks show different values of flux, with higher values in the more blue peak, giving the profiles an asymmetric double-peak shape. The profile of Hδ shows an additional peak at about $1000\,\mathrm{km\,s^{-1}}$ with a nearly similar flux than the blue peak of its profile.
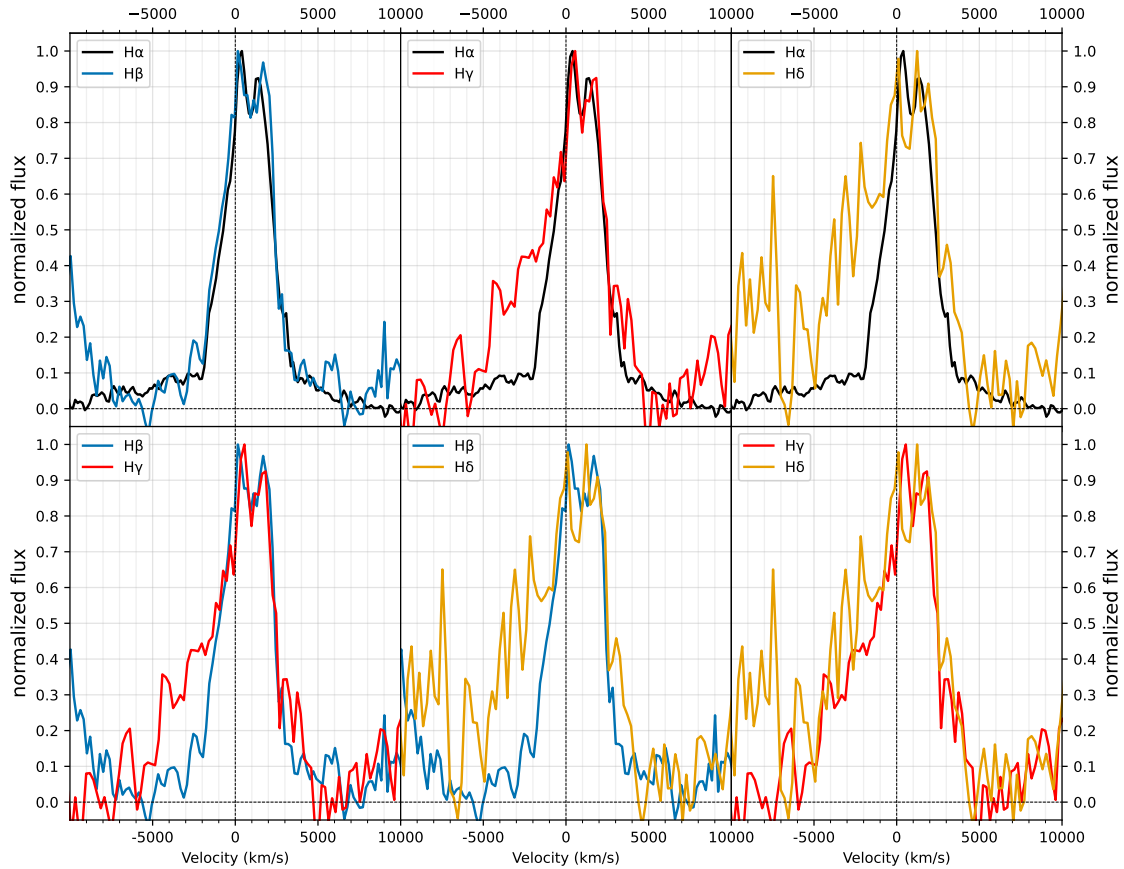

Figure 4.8: Comparison of the normalized RMS line profiles of the Balmer lines Hα, Hβ, Hγ and Hδ.

Looking in more detail into the shape of RMS profiles, the profiles of Hα and Hβ show the most similarity to each other, with both of their flanks following a similar shape. The same applies to the red flanks of Hγ and Hδ with steep slope and a small peak at about $\sim 3000\,\mathrm{km\,s^{-1}}$. Only the blue flank of Hγ and Hδ is more extended and noisy as for Hα and Hβ. This leads to a slightly higher FWHM value for Hγ with $\sim 3900 \pm 400\,\mathrm{km\,s^{-1}}$ compared to the values of Hα and Hβ with $\sim 3100 \pm 250\,\mathrm{km\,s^{-1}}$ and $\sim 3400 \pm 200\,\mathrm{km\,s^{-1}}$ and a much higher value of $\sim 5900 \pm 1000\,\mathrm{km\,s^{-1}}$ for Hδ.

Taking the similarities of the RMS profile shapes, it can be assumed that all four Balmer lines emerge under similar kinematic properties.

Looking at Figure 4.7 it can be seen, that most of the RMS profile is located within the red flank of the AVG profiles, suggesting that a largely part of the measured variation originates at positive velocities of the emitting region.

4.4.3   Helium Line-Profiles

The RMS profiles, as well as a comparison of the He I $\lambda5875$, He II $\lambda4685$ and He II $\lambda1640$ is shown in Figure 4.9. Their RMS profiles are more noisy than the Balmer RMS profiles, due to lower signal to noise ratio, but are still clearly distinguishable from the surrounding continuum.

First looking at the RMS profile of He I $\lambda5875$, shift to positive velocities is noticeable similar to the Balmer RMS profiles, with its maximum located at about $1500\,\mathrm{km\,s^{-1}}$. Going from the maximum, the profile shows a more extended blue flank and a steeper and narrower red flank, with a FWHM of about 4000 ± 400.
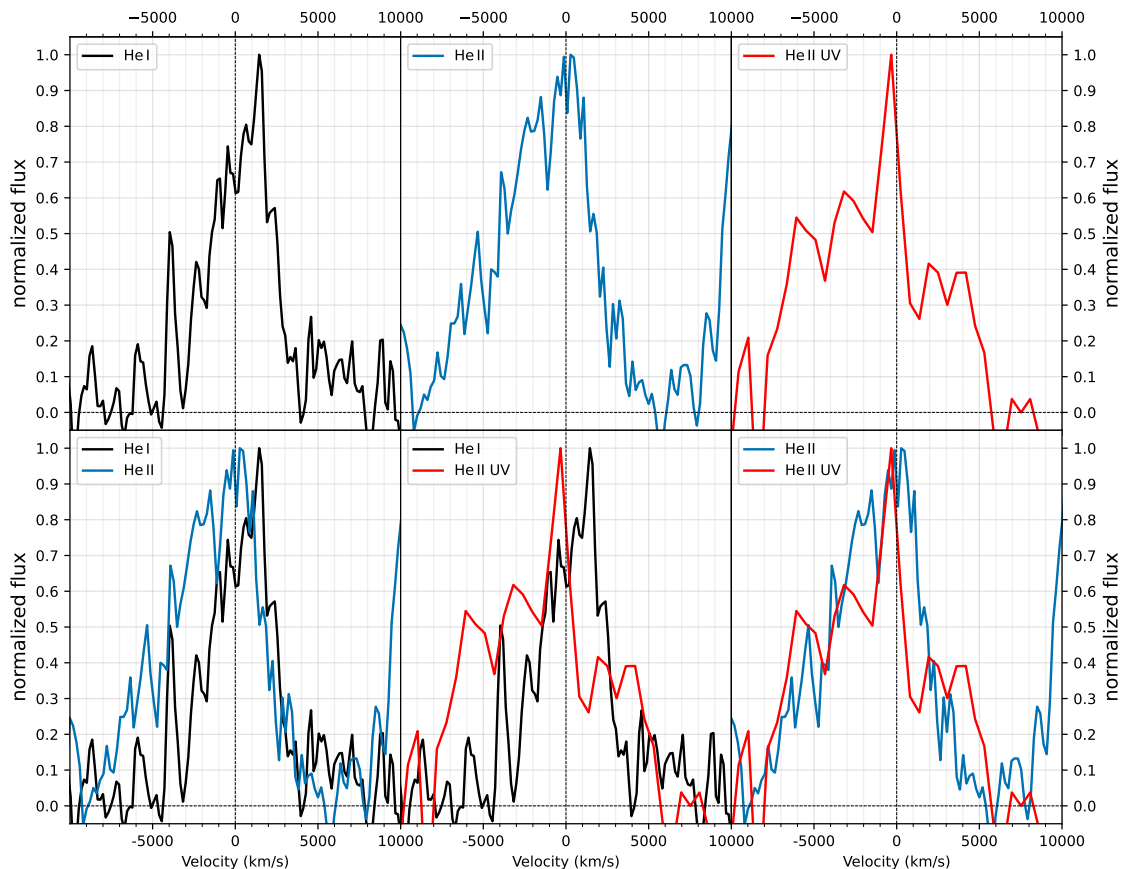

Figure 4.9: Comparison of the normalized RMS line profiles of the Helium lines

A similar shape can be noticed for the RMS profile of He II $\lambda4685$. While its profile is

41

not shifted, like for He I $\lambda 5875$, it also shows a more extended blue flank and narrow red flank, with a FWHM of about $6000 \pm 400 \, \mathrm{km \, s^{-1}}$.

The RMS profile of the UV Helium line He II $\lambda 1640$ is even more noisy, compared to the RMS profiles of the other Helium lines due to its lower signal to noise ratio. Like the He II $\lambda 4685$ RMS profile its maximum is located somewhere around $0 \, \mathrm{km \, s^{-1}}$ and also exhibits a more extended blue flank and a steep slope in its red flank. At around $2000 \, \mathrm{km \, s^{-1}}$ its RMS profile is blended with the RMS profile of semi-forbidden doublet O III] $\lambda\lambda 1660$, 1666. Still, its contribution to the RMS profile of He II $\lambda 1640$ stays below the half height of the profile and does not influence the FWHM measurement with a value of about $6900 \pm 600 \, \mathrm{km \, s^{-1}}$.

Comparing the RMS profiles of the He lines, all three show a similar shape with a extended blue flank and a narrow red flank, with He I $\lambda 5875$ exhibiting a narrower FWHM and a shift towards positive velocities, than the He II RMS profiles, who shows FWHM in the same order of magnitude.

4.4.4 UV Line Profiles

Figure 4.10 shows the RMS profiles of the Lyα line, the N V $\lambda\lambda 1238$, 1242 doublet, the Si IV $\lambda\lambda 1393$, 1402 doublet and the C IV $\lambda\lambda 1548$, 1550 doublet. Starting with Lyα, its RMS profile is blended with line absorption in its blue flank, as well as with the N V $\lambda\lambda 1238$, 1242 doublet in his red flank. Still, its central part is good distinguishable. Similar to the Balmer lines, the most parts, as well as the highest flux is shifted towards positive velocities. It shows a steep blue flank and a slightly broader red flank, which a small broadening at about half height, resulting in a FWHM of about $\sim 4500 \pm 350 \mathrm{km \, s^{-1}}$.

The RMS profile of the neighboring N V $\lambda\lambda 1238$, 1242 doublet is blended with absorption as well as with the Lyα RMS profile. This makes its RMS profile difficult to distinguish. Still it was attempted to estimate its FWHM by taking the width of the red flank of the central peak, resulting in an FWHM of about 3383 ± 1000.

The RMS profile Si IV $\lambda\lambda 1393$, 1402 doublet shows a very broad and scattered profile and is blended with the semi-forbidden line doublet OIV] $\lambda\lambda 1397$, 1400. This leads to a very broad FWHM of about $\sim 10000 \pm 1000 \mathrm{km \, s^{-1}}$. Due to the noise profile and because of a possible interference with the OIV] $\lambda\lambda 1397$, 1400 doublet, the measured FWHM value will not taken into account for the subsequent analysis as well.

Finally, the RMS profile of the C IV $\lambda\lambda 1548$, 1550 doublet shows a very asymmetric profile with a broad plateau like blue wing, with flux staying below half height of the maximum until about $-3000 \mathrm{km \, s^{-1}}$. The center of the RMS profile is shows a

double-peak-like shape with a narrower blue peak and a broader red peak. They are located at about $\sim -1500\,\text{km}\,\text{s}^{-1}$ and $250\,\text{km}\,\text{s}^{-1}$, with higher flux in the red peak. Between the peaks the flux drops below half of the maximum which is why the left flank of the blue peak and the right flank of the red peak has been used to measure the FWHM.
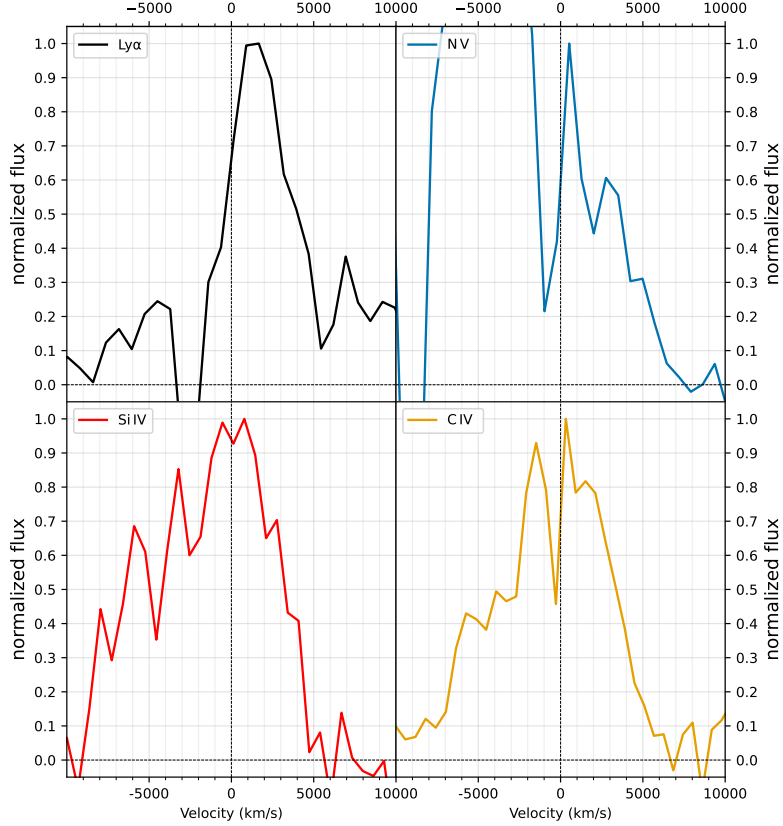

Figure 4.10: Comparison of the normalized RMS line profiles of the UV lines

4.5 Time Lag

The time lag of the measured emission lines relative to the ionizing continuum is determined from the lag between the emission-line light curve and the UVW2 light curve. In section 4.3 it has already been discussed, that it is common to use the most blue continuum as a reference as a proxy for the ionized continuum. By using the Swift UVW2 light curve with an effective wavelength of $\sim 1930,\text{Å}$, the lag between the two continua must be therefore added to the emission-line lag estimate. The time lag between two lightcurves is measured, by determining the cross-correlation function (CCF) of these curves and measuring the centroid of the CCF for values above 80% of the peak, as described in Section 2.2.2. This calcula-

43
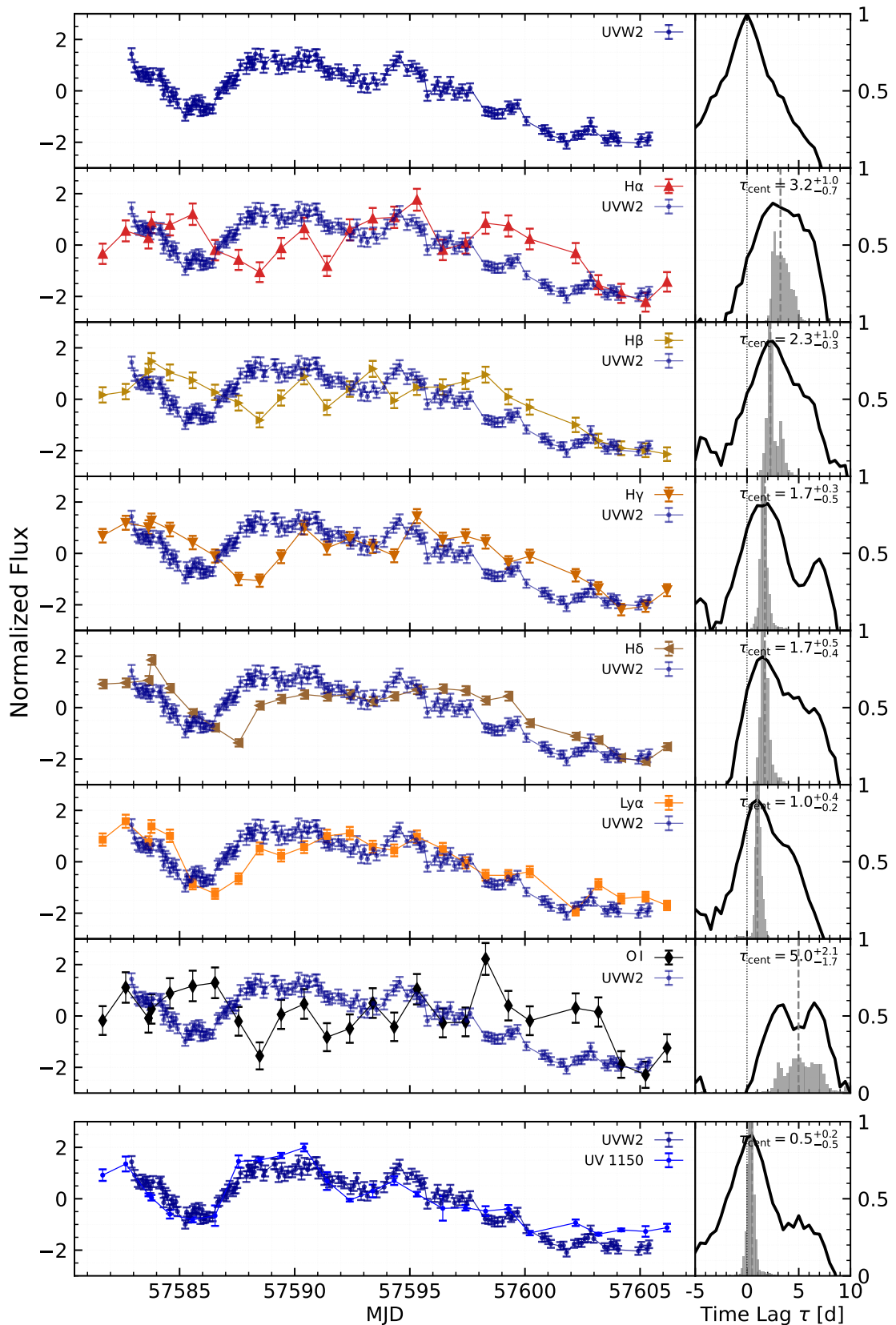
Figure 4.11: Compared lightcurves and CCFs Hα, Hβ, Hγ, He I λ5875, He II λ4685 and O I λ8446 with UVW2 as reference lightcurve.
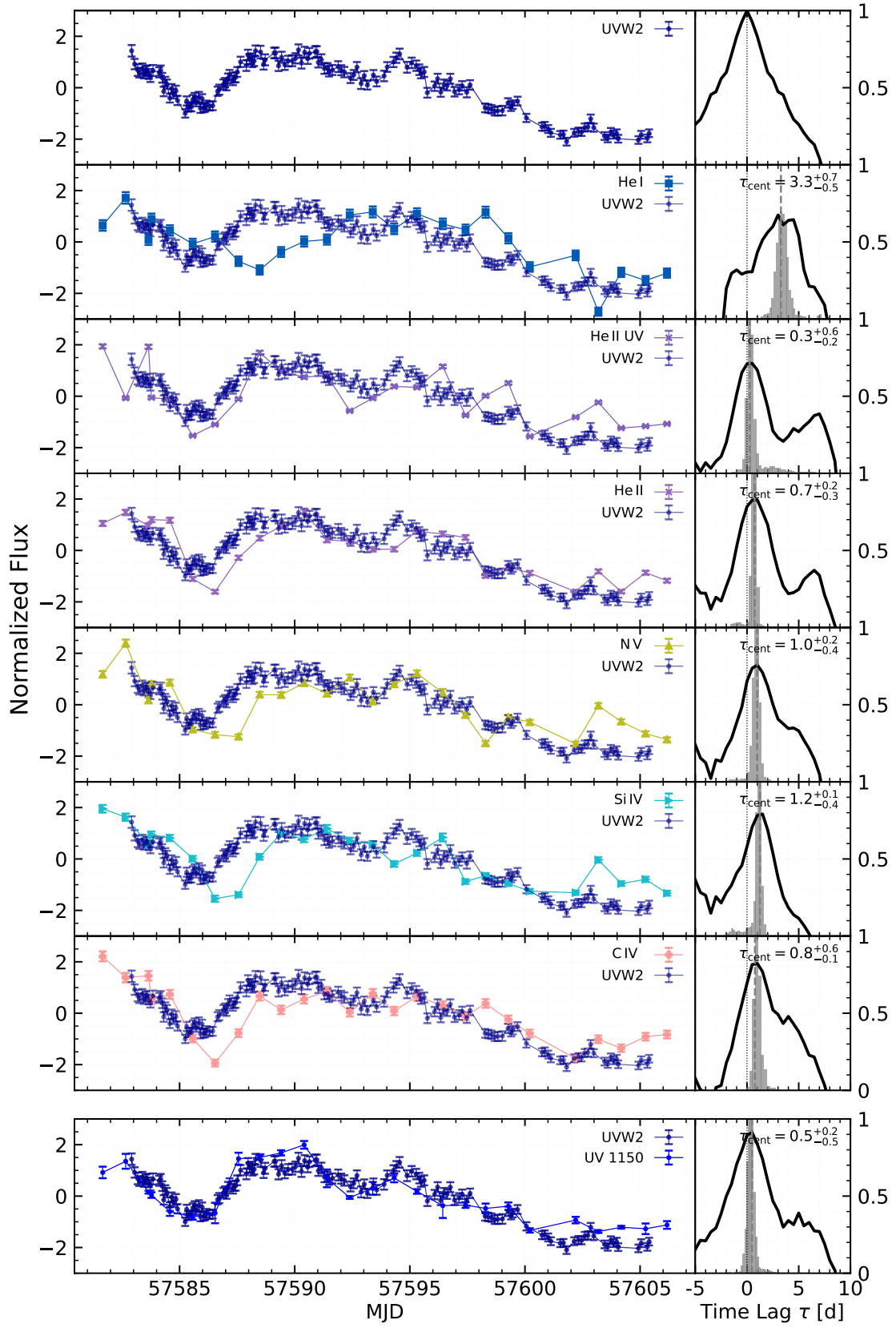
Figure 4.12: Compared lightcurves and CCFs of UV lines with UVW2 as reference lightcurve.

tion is done with GECHO, which applies the interpolated cross-correlation function (ICCF) method introduced by Gaskell & Peterson 1987. The emission-line and reference light curves are normalized by subtracting the respective mean value from each data point. To increase the effective sampling and to measure the correlation between two unevenly sampled light curves, flux values between data points are linearly interpolated for both light curves. The normalized light curves and the resulting CCFs are presented in Figures 4.11 and 4.12. Additionally, the top panel of each figure displays the UVW2 light curve together with its auto-correlation function, while the bottom panel compares both lightcurves of the UVW2 and the UV continuum around 1150 Å and shows the corresponding CCF. The resulting time lags between the UVW2 continuum and each light curve are listed in Table 4.6. The centroid uncertainties are estimated using the flux randomization/random subset selection (FR/RSS) method described by Peterson et al. 1998, with 10000 iterations and a lag bin size of 0.5 days (see Section 2.2.2). The resulting centroid distribution is displayed by the gray histogram in the above named figures.

Overall, the CCFs of all measured emission lines show strong correlations with pronounced peak values between ~ 0.7 and ~ 0.9, except for the CCF of O I 8446, which exhibits two local maxima at values of around ~ 0.6. The two He II lines shows the shortest lag relative to the UVW2 light curve, with an average lag of approximately ~ 0.5 days within the uncertainties. He II,4685 shows a higher peak correlation of approximately ~ 0.8 compared to He II,1640, which reaches values of around ~ 0.7. The CCFs of the other UV emission lines Lyα, N V 1238, Si IV 1393 and C IV 1548 peak at values above ~ 0.8, with Lyα reaching a maximum of approximately ~ 0.9. All of these lines show similar lags of about ~ 1 day within their uncertainties. The Balmer lines exhibit larger lags. Hα and Hβ lag behind the UVW2 light curve by $3.2^{+1.0}_{-0.6}$ and $2.3^{+1.0}_{-0.3}$ days, respectively, while Hγ and Hδ show shorter lags of $1.7^{+0.2}_{-0.4}$ and $1.7^{+0.4}_{-0.4}$ days. Among the Balmer lines, Hβ shows the highest peak correlation, exceeding ~ 0.85, whereas Hα exhibits the lowest correlation, with values of around ~ 0.8. Compared to Hγ and Hδ, the CCFs of Hα and Hβ exhibit broader peaks and wider centroid distributions with larger uncertainties and slightly higher time lag values. He I 5875 and O I 8446 show the lowest correlations with the UVW2 light curve, with peak values of approximately ~ 0.7 and ~ 0.6, respectively. He I 5875 shows a lag of $3.3^{+0.7}_{-0.4}$ days, which is of the same order as the lags measured for Hα and Hβ within the uncertainties. while O I 8446 exhibits the longest lag of $5.0^{+2.1}_{-1.7}$ days relative to UVW2, with large uncertainties caused by the comparatively low CCF peak correlation.

Table 4.6: Centroid and Peak Time Lag for UVW2.

Line	τ_{cent} [d]	Line	τ_{cent} [d]
Hα	$3.2^{+1.0}_{-0.6}$	He I 5875	$3.3^{+0.7}_{-0.4}$
Hβ	$2.3^{+1.0}_{-0.3}$	He II 1640	$0.3^{+0.6}_{-0.2}$
Hγ	$1.7^{+0.2}_{-0.4}$	He II 4685	$0.7^{+0.1}_{-0.3}$
Hδ	$1.7^{+0.4}_{-0.4}$	Si IV 1393	$1.2^{+0.1}_{-0.4}$
Lyα	$1.0^{+0.4}_{-0.2}$	N V 1238	$1.0^{+0.2}_{-0.4}$
O I 8446	$5.0^{+2.1}_{-1.7}$	C IV 1548	$0.8^{+0.5}_{-0.1}$

4.6 Bowen Fluorescence of O I $\lambda 8446$

Emission lines in the optical range, like the Balmer and helium lines, are commonly used in many reverberation-mapping campaigns, as they are easily accessible for nearby AGN (Ochmann et al. 2026). Other lines, such as the low-ionization line O I $\lambda 8446$, have not been of major interest in such campaigns, mostly because of observational limitations (Ochmann et al. 2026). This is why the variability of the O I $\lambda 8446$ line in this campaign is of particular interest, as the line can be enhanced by Bowen fluorescence, pumped by Lyβ emission (Grandi 1980). The time delay between the ionizing continuum and O I $\lambda 8446$ should be consistent with a time delay in which continuum variations drive Lyβ variations, which in turn drive part of the O I $\lambda 8446$ response. Unfortunately, Lyβ lies outside the spectral range of the Cackett et al. 2018 campaign. However, because the Lyα and Lyβ lines are expected to originate under similar physical conditions (Ochmann et al. 2026), Lyα can be used as a proxy for Lyβ. Hα is used to investigate the location of the O I $\lambda 8446$ emitting region relative to the Balmer-line emitting region.

Therefore, the time lags between the UVW2 and emission-line lightcurves, as well as the CCFs and time lags between O I, $\lambda 8446$ and Lyα, between Hα and Lyα, and between O I $\lambda 8446$ and Hα, are calculated and shown in Figure 4.13. All lightcurve show a strong correlation between $\sim 0.75 - 0.8$, with the exception of the O I $\lambda 8446$ and UVW2 lightcurves, which show a maximum correlation of only 0.6. The time lags and their uncertainties are calculated as before. O I $\lambda 8446$ lags behind Lyα by $2.5^{+1.8}_{-0.4}$ days and behind UVW2 by $5.0^{+2.1}_{-1.7}$ days, while Hα lags behind Lyα by $1.8^{+0.5}_{-0.5}$ days and behind UVW2 by $3.2^{+1.0}_{-0.7}$ days. A difference in the response time of about 0.5–1 days between O I $\lambda 8446$ and Hα is noticeable, but are not significant within the uncertainties. Looking at the O I $\lambda 8446$ and Hα lightcurves, they also show a strong correlation, with O I $\lambda 8446$ lagging behind Hα by about $0.3^{+2.0}_{-0.1}$ days. With the Lyα light curve lagging behind the UVW2 light curve by $1.0^{+0.4}_{-0.2}$ days, the total lag along the Bowen-fluorescence path from UVW2 to Lyα and from Lyα to O I $\lambda 8446$ sums

to ~ 3.5 days, which lies within the uncertainties of the time lag between the Hα and UVW2 light curves.
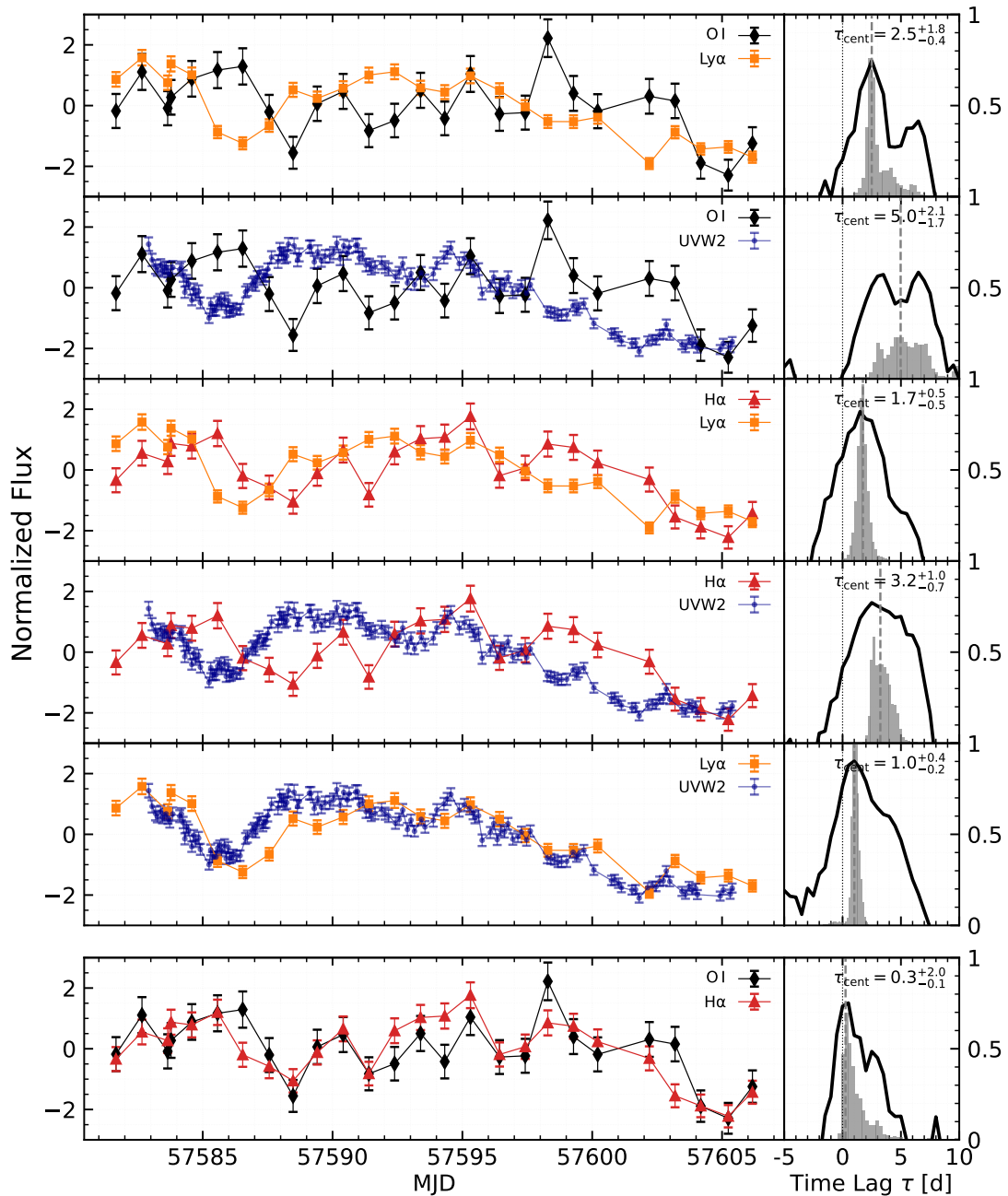

Figure 4.13: Compared lightcurves and CCFs for Bowen Fluorescence.

4.7 Black Hole Mass

The final step of the RM analysis it now the estimation of mass of the SMBH. To do that, the virial theorem get applied following the method of Peterson et al. 2004. The FWHM of the RMS profiles is used to describe the velocity dispersion ΔV which is why a value of $f = 1.8$ gets assumed for the scale factor following Probst et al. 2025 (see Section 2.2.3). Taking equation 2.7, 2.8 and 2.9 the SMBH mass can be estimated based on the time lag and FWHM of for each emission line using:

$$M_{\text{BH}} = 1.8 \cdot \frac{c \cdot \tau_{\text{centroid}} \, \text{FWHM}^2}{G} \, . \tag{4.8}$$

As discussed in Section 4.4, O I $\lambda 8446$, and Si IV $\lambda\lambda 1238$, 1242 are not included, due to not measurable or significant FWHM values. The resulting SMBH mass results, as well as the corresponding time lag and FWHM values of the broad emission lines are listed in Table 4.7. To obtain a final estimation for the SMBH mass, a inverse-variance weighted mean is calculated. Since the uncertainties are asymmetric the higher gets adopter, $\sigma_i = \max(\sigma_i^-, \sigma_i^+)$. The weighted mean is then given by

$$\bar{M}_{\text{BH}} = \frac{\sum_i w_i M_{\text{BH},i}}{\sum_i w_i} \, , \qquad w_i = \frac{1}{\sigma_i^2} \, , \tag{4.9}$$

with an uncertainty

$$\sigma_{\bar{M}} = \left(\sum_i w_i \right)^{-1/2} \, . \tag{4.10}$$

This yields the weighted-mean SMBH mass of $\bar{M}_{\text{BH}} \approx (0.89 \pm 0.16) \times 10^7 \, M_\odot$.

It has to be noted, that the scale factor of $f = 1.8$ does not account the low-inclination $i \sim 11°$ of the elliptic accretion disk, modeled in Ochmann et al. 2024. Adopting the scaling relation $f \sim \sin^{-2}(i)$ introduced by Krolik 2001, a value of $f \sim 27.5$ would be needed to account for the low inclination. Krolik 2001 used the line dispersion to parameterize the velocity dispersion, which is why the relation $\sigma_{\text{line}} \approx \text{FWHM}/2$ (Peterson et al. 2004) has to be accounted again. Due to the square relation of the velocity dispersion to the black hole mass seen in Equation 4.8, the scale factor finally gets corrected to a value $f \sim 6.8$. Subsequently the found BH mass has to be multiplied by a additional factor of 3.77.

Subsequently, the weighted-mean SMBH mass yields $\bar{M}_{\text{BH,corr}} \approx (3.35 \pm 0.62) \times 10^7 \, M_\odot$.

Table 4.7: Estimated time lags, FWHM and SMBH masses.

Line	τ_{cent} [d]	FWHM (rms)[km/s]	$M_{\mathrm{BH}}[10^7 M_\odot]$
Lyα	$1.0^{+0.4}_{-0.2}$	4566 ± 150	$0.7^{+0.3}_{-0.2}$
Hα	$3.2^{+1.0}_{-0.6}$	3111 ± 250	$1.1^{+0.6}_{-0.4}$
Hβ	$2.3^{+1.0}_{-0.3}$	3437 ± 200	$0.9^{+0.6}_{-0.2}$
Hγ	$1.7^{+0.2}_{-0.4}$	3852 ± 300	$0.9^{+0.3}_{-0.3}$
Hδ	$1.7^{+0.4}_{-0.4}$	5905 ± 1000	$1.5^{+0.6}_{-0.5}$
He I $\lambda 5876$	$3.3^{+0.7}_{-0.4}$	3952 ± 300	$1.8^{+0.7}_{-0.5}$
He II $\lambda 1640$	$0.3^{+0.6}_{-0.2}$	6891 ± 600	$0.4^{+1.2}_{-0.3}$
He II $\lambda 4686$	$0.7^{+0.1}_{-0.3}$	5972 ± 300	$0.9^{+0.2}_{-0.4}$
N V $\lambda 1238$	$1.0^{+0.2}_{-0.4}$	3383 ± 1000	$0.4^{+0.4}_{-0.3}$
C IV $\lambda\lambda 1548, 1550$	$0.8^{+0.5}_{-0.1}$	8428 ± 300	$1.9^{+1.7}_{-0.2}$

5. Discussion

Bibliography

Aladin Lite (2025). CDS (Centre de Données astronomiques de Strasbourg). URL: https://aladin.cds.unistra.fr/AladinLite/ (visited on 07/19/2025).

Anderson, J. & L. R. Bedin 2010, *Publications of the Astronomical Society of the Pacific*, 122, 1035.

Antonucci, Robert 1993, *Annual Review of Astronomy and Astrophysics*, 31, 473–521.

Beckmann, Volker & Chris R. Shrader 2013, *The AGN phenomenon: open issues*, URL: https://arxiv.org/abs/1302.1397.

Bowen, I. S. 1934, *Publications of the Astronomical Society of the Pacific*, 46, 146–148.

Bowen, I. S. 1947, *Publications of the Astronomical Society of the Pacific*, 59, 196.

Cackett, E. M., M. C. Bentz, & E. Kara 2021, *iScience*, 24, 102557.

Cackett, E. M., C.-Y. Chiang, I. McHardy, et al. 2018, *The Astrophysical Journal*, 857, 53.

Denney, K. D., M. C. Bentz, B. M. Peterson, et al. 2006, *Astrophysical Journal Letters*, 653, 152–158.

Dexter, J. & E. Agol 2010, *The Astrophysical Journal*, 727, L24.

Gaskell, C. M. & B. M. Peterson 1987, *The Astrophysical Journal Supplement Series*, 65, 1.

Goad, M. R., K. T. Korista, & A. J. Ruff 2012, *Monthly Notices of the Royal Astronomical Society*, 426, 3086–3111.

Graham, A. W., C. A. Onken, E. Athanassoula, et al. 2011, *Monthly Notices of the Royal Astronomical Society*, 412, 2211–2228.

Grandi, S. A. 1980, *The Astrophysical Journal*, 238, 10.

Grier, C. J., P. Martini, L. C. Watson, et al. 2013, *The Astrophysical Journal*, 773, 90.

Horne, K., B. M. Peterson, S. J. Collier, et al. 2004, *Publications of the Astronomical Society of the Pacific*, 116, 465.

Hubble Advanced Spectral Products (HASP) (2025). Space Telescope Science Institute. URL: https://archive.stsci.edu/missions-and-data/hst/hasp (visited on 09/17/2024).

Institute, Space Telescope Science (2025). *STIS Instrument Handbook: Gratings.* URL: https://hst-docs.stsci.edu/stisihb/chapter-13-spectroscopic-reference-material/13-3-gratings (visited on 05/12/2025).

Keel, Bill (2002). *Quasars and Active Galactic Nuclei - Optical spectra of various kinds of active galactic nuclei.* Accessed: 2025-12-22. URL: https://pages.astronomy.ua.edu/keel/agn/spectra.html.

Kollatschny, W. & M. Dietrich 1997, *Astronomy and Astrophysics*, 323, 5–13.

Koss, M. J., C. Ricci, B. Trakhtenbrot, et al. 2022, *The Astrophysical Journal Supplement Series*, 261, 2.

Krolik, Julian H 2001, *The Astrophysical Journal*, 551, 72.

McHardy, I. M., S. D. Connolly, B. M. Peterson, et al. 2017, *Monthly Notices of the Royal Astronomical Society*, 465, 273–289.

McHardy, IM, SD Connolly, K Horne, et al. 2018, *Monthly Notices of the Royal Astronomical Society*, 480, 2881–2897.

Mikulski Archive for Space Telescopes (MAST) (2025). Space Telescope Science Institute. URL: https://mast.stsci.edu/search/ui/#/hst (visited on 09/17/2024).

Mo, H., F. van den Bosch, & S. White 2010, *Galaxy Formation and Evolution*, Cambridge University Press.

Netzer, H. 2013, *The Physics and Evolution of Active Galactic Nuclei*, Cambridge University Press, Cambridge.

Netzer, H. & M. V. Penston 1976, *Monthly Notices of the Royal Astronomical Society*, 174, 319–325.

Ochmann, M. W., W. Kollatschny, M. A. Probst, et al. 2024, *Astronomy & Astrophysics*, 686, A17.

Ochmann, M. W., P. M. Weilbacher, M. A. Probst, et al. 2025, *Astronomy & Astrophysics*, 697, L5.

Ochmann, Martin W, Edward M Cackett, Lukas Diehl, et al. 2026, *Astronomy and Astrophysics*, 705, L11.

Onken, C. A., L. Ferrarese, D. Merritt, et al. 2004, *The Astrophysical Journal*, 615, 645–651.

Osterbrock, D. E. 1977, *The Astrophysical Journal*, 215, 733–745.

Osterbrock, D. E. 1981, *The Astrophysical Journal*, 249, 462–470.

Osterbrock, Donald E. & Richard W. Pogge 1985, *The Astrophysical Journal*, 297, 166–176.

Peterson, B. M. 1993, *Publications of the Astronomical Society of the Pacific*, 105, 247–268.

Peterson, B. M. 1997, *An Introduction to Active Galactic Nuclei*, Cambridge University Press.

Peterson, B. M., L. Ferrarese, K. M. Gilbert, et al. 2004, *The Astrophysical Journal*, 613, 682–699.

Peterson, B. M. & K. Horne 2004, *Astronomische Nachrichten*, 325, 248–251.

Peterson, B. M., I. Wanders, K. Horne, et al. 1998, *Publications of the Astronomical Society of the Pacific*, 110, 660.

Peterson, Bradley M. 2011, *Masses of Black Holes in Active Galactic Nuclei: Implications for NLS1s*, URL: https://arxiv.org/abs/1109.4181.

Probst, M. A., W. Kollatschny, M. W. Ochmann, et al. 2025, *Emission-Line and Continuum Reverberation Mapping of the NLS1 Galaxy WPVS 48*, URL: https://arxiv.org/abs/2511.09153.

Rees, M. J. 1984, *Annual Review of Astronomy and Astrophysics*, 22, 471–506.

Ricci, C. & B. Trakhtenbrot 2023, *Nature Astronomy*, 7, 1282–1294.

Rodriguez-Pascual, PM, D Alloin, J Clavel, et al. 1997, *The Astrophysical Journal Supplement Series*, 110, 9.

Seyfert, Carl K. 1943, *The Astrophysical Journal*, 97, 28–40.

Shakura, N. I. & R. A. Sunyaev 1973, *Astronomy and Astrophysics*, 24, 337–355.

STScI (2025). *Digitized Sky Survey*. IPAC. DOI: 10.26131/IRSA441. URL: https://www.ipac.caltech.edu/doi/irsa/10.26131/IRSA441 (visited on 07/19/2025).

Ulrich, M.-H., L. Maraschi, & C. M. Urry 1997, *Annual Review of Astronomy and Astrophysics*, 35, 445–502.

Urry, C. M. & P. Padovani 1995, *Publications of the Astronomical Society of the Pacific*, 107, 803–845.

A. Additional Tables

Table A.1: Dispersion of grating in velocity space.

Line	Dispersion $[\frac{km}{s}/\text{pixel}]$
Lyα	144.0
Hα	222.9
Hβ	169.3
Hγ	189.6
Hδ	200.6
He I λ5875	249.0
He II λ1640	106.7
He II λ4685	175.6
N V $\lambda\lambda$1238, 1242	141.3
Si IV $\lambda\lambda$1238, 1242	125.6
C IV $\lambda\lambda$1548, 1550	113.1